

Coatings and clusters of carboxylic acids in carbon-containing atmospheric particles from spectromicroscopy and their implications for cloud-nucleating and optical properties

S. Takahama,¹ S. Liu,¹ and L. M. Russell¹

Received 10 June 2009; revised 6 August 2009; accepted 21 August 2009; published 8 January 2010.

[1] Particle shape and distribution of chemical compounds within individual particles are implied in the parameterizations used in air quality and climate models for radiative transfer, volatility, and mass transfer. In this study we employ Scanning Transmission X-Ray Microscopy with Near-Edge X-Ray Absorption Fine Structure Spectroscopy with image analysis and pattern recognition techniques to characterize the chemical structure of 636 particles collected on six field campaigns in the western hemisphere between 2004 and 2008. Many of the particles were chemically heterogeneous. A few observed types include black carbon particles covered by aqueous-phase components ($n = 90$), dust particles with organic clumps (106), organic particles enriched in carboxylic acid at the surface (54), and inorganic cores encapsulated by organic shells (10). The 90 particles in the first category collectively contained 95 regions showing a strong black-carbon spectral signature associated with the aqueous-phase components, of which 78 were between 0.1 and 1 μm . Organic mass fraction of the organic dust particles varied significantly (mean and standard deviation of 0.3 ± 0.2), and over half of these dust particles were found to be nearly spherical. Thickness of acid-enriched coatings and carbon on inorganic cores were less than 0.6 μm in most cases, but accounted for <0.01 to 0.98 of the particle volume fraction. More than half of the identified organic particles (359) were found to be chemically heterogeneous, and 32 particles were observed as agglomerations or inclusions but did not meet one or more of the criteria of the categories described here. The acidic coatings on black carbon are calculated to have a significant impact on the critical supersaturation of these particles. The measured distribution of aspect ratios of dust and other particles in our samples ranged nonuniformly between 1.0 and 4.6 with a mean of 1.4, which can affect assessment of extinction-to-backscatter ratios over the case where spherical geometry is assumed.

Citation: Takahama, S., S. Liu, and L. M. Russell (2010), Coatings and clusters of carboxylic acids in carbon-containing atmospheric particles from spectromicroscopy and their implications for cloud-nucleating and optical properties, *J. Geophys. Res.*, 115, D01202, doi:10.1029/2009JD012622.

1. Introduction

[2] Atmospheric particles can contain sulfate, ammonium, nitrate, elemental carbon, organic compounds, trace metals, crustal elements, and water [Seinfeld and Pandis, 2006]. Depending on the spatial distribution of these components within individual particles, chemical species found in small portions can have disproportionate effects on aerosol properties relevant to climate [e.g., Bilde and Svenningsson, 2004; Shilling *et al.*, 2007] and health. In addition to being chemically heterogeneous, particles can be present in many types of physical configurations, or morphologies. Most generally the categorization might be spherical and nonspherical (or irregular). Further character-

ization of irregularities may include agglomerations, which are aggregations of more fundamental units, and eccentric inclusions or concentric layers, including encapsulating shells and films. These classifications have some basis in modeling aerosol optical properties [Mishchenko *et al.*, 2002, 2004, 2007], but such physical shapes and chemical distributions within individual particles can also influence the behavior of water uptake, removal, and volatility, with implications for direct radiative forcing, cloud condensation nuclei (CCN) activation properties, and interpretation of measurements and satellite images. For instance, organic films or solid organic particles enclosing water-soluble inorganic components can retard water uptake [Chan and Chan, 2005; Sjogren *et al.*, 2007]. Polar organic coatings can increase the hygroscopicity of the particle, leading to increase in CCN activity [Cruz and Pandis, 1998] and removal rate of particles onto which they are condensed or reacted [Zuberi *et al.*, 2005]. The mixing state and internal configuration of absorbing black carbon can change its optical

¹Scripps Institution of Oceanography, University of California, San Diego, La Jolla, California, USA.

Table 1. Summary of Measurements

Field Campaign	Study Period	Location	Platform	Altitude (m)	Number of Particles
MILAGRO	Mar 2006	Mexico City	urban ground site	2200	109
MILAGRO	Mar 2006	Mexico mainland/Yucatan peninsula	NCAR C-130	2090–4340	83
INTEX-B	May 2006	U.S. West coast	NCAR C-130	890–1920	176
ICEALOT	Mar–Apr 2008	Arctic Sea	NOAA <i>Ronald H. Brown</i>	18	35
Whistler	May–Jun 2008	Whistler, Canada	high-elevation ground site	1020	90
VOCALS REx	Oct–Nov 2008	west coast of South America	NOAA <i>Ronald H. Brown</i>	18	116
Scripps Pier	Sep 2008 to present	San Diego, Calif.	Scripps Institution of Oceanography	15	21

properties [e.g., *Jacobson, 2000; Bond and Bergstrom, 2006*]. Characterizing the sphericity and its variability in a particle ensemble is important for satellite retrievals [*Wang et al., 2003*].

[3] Atmospheric aerosol morphology and chemical composition has previously been observed by other methods, including scanning electron microscopy with electron dispersive X-ray (SEM/EDX) [e.g., *Laskin et al., 2006*], transmission electron microscopy with electron energy loss spectroscopy (TEM-EELS) [e.g., *Katrinak et al., 1992*], and inferred from single-particle mass spectrometry combined with light scattering techniques [e.g., *Moffet et al., 2008*]. Scanning Transmission X-Ray Microscopy with Near-Edge Absorption Fine Structure (STXM-NEXAFS) [*Stöhr, 1992; Kilcoyne et al., 2003*] is a technique with high chemical sensitivity and low radiation damage with respect to electron microscopy methods [*Urquhart et al., 1999; Braun et al., 2005; Alexander et al., 2008; Braun et al., 2009*], and has been used to probe functional group composition in individual particles relevant to the atmosphere [e.g., *Russell et al., 2002; Braun, 2005; Hopkins et al., 2007; Tivanski et al., 2007; Takahama et al., 2007, 2008; Braun et al., 2008*]. The number of particles that can be analyzed by this method is limited by access to a synchrotron radiation facility and the X-ray microscopy end station, but STXM-NEXAFS provides advantages in high chemical resolution and capability for analysis at atmospheric pressure. The objectives of this study are to characterize the physical morphology and chemical heterogeneities of individual carbon-containing particles collected from field campaigns in different geographical locations: MILAGRO (Mexico City and mainland, March 2006), INTEX-B (North American west coast, May 2006), ICEALOT (northern Arctic, March–April 2008), Whistler (Whistler, Canada, May–June 2008), VOCALS REx (Southern Hemisphere, October–November 2008), and in La Jolla, California (September 2008 to March 2009).

2. Methods

2.1. Sample Collection and Analysis

[4] During four field campaigns on five platforms (Table 1), particles were collected on silicon nitride windows (Si_3N_4 ; Silson Ltd.) mounted on a rotating impactor (Streaker; PIXE International, Inc.). Aluminum or copper tubing was used to draw air into the impactor at 1 Lpm ($1.6 \times 10^{-5} \text{ m}^3 \text{ s}^{-1}$); sampling times for each window ranged between 10 and 30 minutes. Samples were frozen after collection, during storage, and in transit until time of analysis (samples were analyzed between June 2006 and April 2009). Sampled grids and windows were analyzed at the Advanced Light Source at Lawrence Berkeley National Laboratories (Berkeley, California) Beamline 5.3.2 in a He-filled chamber main-

tained at 1 atm (dry). Analysis at atmospheric pressure avoids losses by cavitation, which can occur in vacuum or low-pressure environments. A comparison of PM_{10} organic mass characterized by Fourier Transform Infrared Spectroscopy, following a similar storage and transport protocol and analysis in a nitrogen headspace, shows 87–106% of organic mass recovery with respect to an in situ analysis technique (Aerodyne Aerosol Mass Spectrometer) [*Gilardoni et al., 2007; Russell et al., 2009; Gilardoni et al., 2009*]. This comparison serves as an empirical estimate for the magnitude of evaporative losses and artifacts incurred by our established protocols for offline analysis of complex atmospheric particles, which will presumably include organic compounds with equilibrium vapor pressures reduced through mixture effects [e.g., *Cappa et al., 2008*] and oligomerization [e.g., *Jang et al., 2002; Gao et al., 2004; Kalberer et al., 2004; Tolocka et al., 2004; Kroll and Seinfeld, 2008*].

[5] The list of geographic locations, time periods, and number of particles examined from each project is shown in Table 1. Transmission of photons at energy levels between 278 and 320 eV (0.2–5 eV resolution) was measured over a minimum spatial resolution of 30 nm and converted to optical density [*Russell et al., 2002; Tivanski et al., 2007*].

2.2. Image and Spectra Interpretation

2.2.1. Image Processing

[6] Series of transmission images associated with each particle were registered according to a cross-correlation algorithm [*Gonzalez et al., 2003*], conservatively segmented into two regions interpreted as the background (I_0) and foreground (I), and converted to absorbance ($A = -\log(I/I_0)$; also referred to as optical density). “Intensity” is defined here as a value of absorbance or integrated absorbance mapped to an image. Following the application of a median filter to denoise each image, absorbance images at 288.85 eV were segmented and subjected to connected components labeling to define pixel membership and boundaries associated with each particle (in almost all cases, 288.85 eV corresponds to the maximum projected area). A similar method was applied to define regions in which the carbon signal was above detectable limits and unsaturated.

2.2.2. Spectra Interpretation

[7] Average spectra for each particle and for individual spectra were interpreted through peak assignments of functional groups reported in the literature (Table 2). Semiquantitative analysis followed the fitting of functional forms to expected features in the spectra (as described by *Schumacher et al.* [2005], *Hopkins et al.* [2007], and *Takahama et al.* [2007]; functional forms are defined in Table 2). The pre-edge absorbance was quantified (mean value between 278 and 283 eV) and subtracted from each spectrum. The shifted spectrum was then normalized by the carbon K-edge

Table 2. Spectra Interpretation

Description/Interpretation	Functional Form	Nominal Location(s) (eV)
<i>Preedge Features</i>		
Inorganic mass	constant	278–283 ^a
<i>Edge/Near-Edge Features</i>		
Benzoquinone, R(C = C)R'	Gaussian peak ^b	284.0 ^c
Alkene/aromatic, R(C = C)R'	Gaussian peak ^b	285 ^a
Ketonic carbonyl, R(C = O)R	Gaussian peak ^b	286.7 ^a
Alkyl, R(C-H) _n R	Gaussian peak ^b	287.7 ^a
Carboxylic carbonyl, R(C = O)OH	Gaussian peak ^b	288.7 ^a
Amide and/or Alcohol, CNH-COH	Gaussian peak ^b	289.5 ^{a,d}
Carbonate, CO ₃ ²⁺	Gaussian peak ^b	290.4 ^a
Carbon K edge	arctangent	290 ^e
<i>Postedge Features</i>		
σ* transitions	Gaussian peaks (width < 3 and <5 eV FWHM)	294, 303 ^c
Potassium, K ⁺	polygons	297.4, 299.9 ^f
Total carbon	constant	305–320 ^d

^aRussell et al. [2002].^bWidth = 1 eV FWHM.^cBraun [2005].^dTivanski et al. [2007].^eSchumacher et al. [2005].^fYoon et al. [2006].

absorbance (mean value between 305 and 320 eV). The π^* transitions (near-edge absorbance, Table 2) were fitted with Gaussian peaks with a fixed full width at half maximum (FWHM) of 1 eV. Two additional peaks representing σ^* transitions were modeled by two Gaussian peaks located at 294 and 303 eV, with maximum allowed FWHM of 3 and 5 eV, respectively. In addition, a Gaussian peak at 294 eV was simultaneously fitted to represent the contribution from CO₃²⁺. The carbon K edge was modeled as an arctangent function centered at 290 eV. Its fitted contribution to each spectrum was consistent with the expected value of unity of total carbon in the normalized spectra. The contribution from L_{II} and L_{III} edges of potassium were taken into account by excluding energies between 295 and 302 in the fitting [Schumacher et al., 2005].

2.2.3. Geometric Parameters

[8] The projected-area-equivalent sphere diameter is defined as the diameter of a circle with the same area as the projected image. The aspect ratio is defined as $\max(a, b)/\min(a, b)$ where (a, b) are the dimensions of the box which bounds the particle (oriented along the ellipse-equivalent major axis). Estimated uncertainties for these values consider both the image(s) used in defining the particle boundaries and the image segmentation algorithm. Minimum and maximum values are computed from examining the union and intersection of binary images for multiple energies (>288 eV) near and after the carbon K edge; and the segmentation algorithms considered were the interregion variance maximization method [Otsu, 1975] and *K*-means clustering [Hastie et al., 2005].

2.2.4. Texture Analysis

[9] The uniformity of integrated peak areas for specific components (which presumably corresponds to the distribution of the associated chemical group) is assessed by means of cooccurrence matrix $\mathbf{C} = [c_{ij}]$ [Haralick et al., 1973], expressed as

$$c_{ij} = |\{(p, q) \in P \times Q : Z(\mathbf{r}_p) = i \vee Z(\mathbf{r}_p + (\Delta\mathbf{r})_q) = j\}|.$$

$Z(\mathbf{r}_p)$ is the value of the scalar field Z at pixel location \mathbf{r}_p ; P is the set of all foreground pixels belonging to the particle of interest. Z is obtained through transformation of intensities into eight indices. $(\Delta\mathbf{r})_q$ is the q th offset distance, and Q is the vector pointing omnidirectionally (0 to 315° in 45° increments) from the reference pixel. $|X|$ is the cardinality (number of elements) of a set X . The matrix is normalized to the total number counts to approximate a probability density $p(i, j)$ for intensity cooccurrence, and a contrast parameter is extracted from this matrix as $\sum_{i,j} (i - j)^2 p(i, j)$. The contrast parameter indicates the variation in intensity across a structuring element ($\{(\Delta\mathbf{r})_q, q \in Q\}$). A constant image would have a contrast of zero, while images with widely varying intensities over length scales probed by the structuring element would have a high contrast value. This calculation was repeated for distances 1, 3, 5, 10, and 15 pixel units away for each particle to examine the change in contrast parameter with distance. Since STXM-NEXAFS is a transmission method, the textural analysis does not correspond to analysis of “surface” textures, but the application of this algorithm is intended to further characterize spatial patterns in image intensity to the extent permitted by the spatial resolution (0.03–0.3 μm) of our images.

2.3. Pattern Recognition Methods

2.3.1. Factor Analysis

[10] A 3-D $p \times q \times n$ array is collapsed to a matrix, $\mathbf{X} = [x_{ij}]$, of dimensions $m \times n$, where $m = p \times q$. To decompose \mathbf{X} into a sum of linear components and their contributions ($\mathbf{F} = [f_{kj}]$ and $\mathbf{G} = [g_{ik}]$, respectively), Positive Matrix Factorization (PMF) [Paatero and Tapper, 1994] was used:

$$\begin{aligned} \{\mathbf{G}, \mathbf{F}\} &= \arg \min_{\mathbf{G}, \mathbf{F}} \sum_{i=1}^m \sum_{j=1}^n w_{ij} e_{ij}^2 \\ \text{s.t. } e_{ij} &= x_{ij} - \sum_{k=1}^p g_{ik} f_{kj} \quad \forall i = 1, \dots, m \\ g_{ik} &\geq 0, f_{kj} \geq 0 \quad j = 1, \dots, n \\ &\quad k = 1, \dots, h. \end{aligned} \quad (1)$$

We define a matrix of weights $\mathbf{w} = [w_{ij}] = \mathbf{1}$ to consider absorbances at all energy levels and pixels equally (though optically dense regions with less relative uncertainties will naturally impose greater influence on the fitting). This choice of weighting matrix is consistent with the assessment of spectral similarity by the Euclidean distance metric for cluster analysis (discussed below). The advantage of this matrix decomposition method over others is that its application does not require centering and scaling of the data, and its nonnegativity constraint leads to component profiles that can be physically meaningful [Paatero and Tapper, 1994]. Its advantage as a factor analytic technique is highlighted when considering that Lerotic *et al.* [2004] similarly examined chemical distributions over images using principal components analysis, but only as an initial data reduction and smoothing technique because the principal components or factors could not be interpreted. The number of factors, h , must be specified in obtaining a solution to equation (1); two- and three-component solutions are sought as increasing the number of factors further leads to colinear solutions in most cases. A rotational degree of freedom is permitted when obtaining a solution from PMF, as equation (1) does not specify enough constraints for unique determination of the matrices \mathbf{G} and \mathbf{F} . Therefore, a set of possible solutions are generated through the variation of a rotational parameter, FPEAK [Paatero *et al.*, 2002]. For this study, we choose a parameter of FPEAK = -0.2 as this rotation appeared to produce the most plausible component profiles in almost every case. Plausibility is established through comparison of profile spectra with average particle spectra: assuming that there exists some number of average particle spectra that display characteristics of “pure-component” spectra, plausible component profiles qualitatively resemble a subset of average particle spectra found in this study and also those reported by Takahama *et al.* [2007].

2.3.2. Cluster Analysis

[11] Cluster analysis is performed on a distance matrix $\mathbf{D} = [d_{ij}]$. If \mathbf{x}_i and \mathbf{x}_j are the i th and j th row vectors of \mathbf{X} , respectively, the elements of \mathbf{D} are defined as $d_{ij} = d(\mathbf{x}_i, \mathbf{x}_j)$. The distance function d was defined by the 2-norm (Euclidean) distance ($\|\mathbf{x}_i - \mathbf{x}_j\|_p$ where $p = 2$). No normalization to the spectra prior to clustering was applied. An agglomerative hierarchical clustering algorithm that minimizes the error sum of squares relative to cluster centers [Ward, 1963] was used to select group membership. It has been suggested [e.g., Lerotic *et al.*, 2005] that while routinely applied, clustering image pixels by Euclidean distance can lead to stratification simply by optical density rather than chemical differences. In our experience, particle regions with significant spectral differences can still be identified with this choice of distance metric, while for sufficiently homogeneous particles the stratification indeed appears to occur arbitrarily by thickness, as suggested. Results from clustering by Euclidean distance were compared with results from 1-norm (Manhattan) distance and the angle distance measure [or normalized scalar product, $\cos^{-1}(\mathbf{x}_i^T \mathbf{x}_j / (\|\mathbf{x}_i\|_2 \cdot \|\mathbf{x}_j\|_2))$] [Lerotic *et al.*, 2005], and were found to be qualitatively similar; Pearson’s correlation coefficient (employed as a distance metric) did not perform as well in the grouping task as determined by comparison of clustered spectra. Therefore, clustering results based on the

Euclidean norm distance are selected for discussion in the rest of this manuscript.

2.3.3. Classification

[12] Average spectra for each particle and also spectra associated with individual pixels from every particle were classified according to the k -nn algorithm and a training set constructed from spectra reported by Takahama *et al.* [2007]. To briefly summarize, this training set consists of 14 types grouped on basis of relative functional group abundances. These 14 types are regrouped into several metaclasses: three of these metaclasses were determined on the basis of similarity with source spectra reported in the literature (combustion, ultisol soil, and biomass burning), and a spectra type dominated by a carboxylic carbonyl signature was additionally labeled as “secondary” to indicate that they may have been formed through gas-phase oxidation reactions of volatile organic compounds (carboxylic acids are large constituents of secondary organic aerosol). “Ultisol” is a type of soil from Puerto Rico exhibiting strong absorbances for the carboxylic carbonyl, carbonate, and potassium in its NEXAFS spectra [Ade and Urquhart, 2002] and for which we find many similar atmospheric particle spectra [Takahama *et al.*, 2007; Leaitch *et al.*, 2009]; we consider these particles a subset of dust particles in the atmosphere. The remaining types not included in one of these four metaclasses are categorized as “other”. Prior to classification, spectra were normalized by subtracting preedge absorbance and dividing by the mean (equivalent to normalizing by the $\|\mathbf{x}_i\|_1$ absorbance, where \mathbf{x}_i is either the average absorbance spectrum or absorbance spectrum from a single pixel) for energy levels below 295 eV to focus on near-edge functional group features, as similar preprocessing was applied to create the original categories.

2.4. Groups and Morphologies

2.4.1. Morphological Characterization

[13] Particles are classified into categories of spherical or nonspherical. Particle sphericity is established if a coefficient of determination (R^2) of a linear model, which assumes radial distribution of intensity for a spherical particle, was greater than 0.6. The thickness of a sphere with radius R_p as a function of radial distance r is

$$t(r) = 2 R_p \sin(\cos^{-1}(r/R_p)). \quad (2)$$

Therefore, a model is fit in which the absorbance is linearly related to the sample thickness,

$$A_i = \sigma t_i + \epsilon_i \quad \forall i \in P, \quad (3)$$

where i denotes the index of P , the set of foreground pixels, A_i is the 288.85 eV absorbance, ϵ_i is the error term, and t_i is the thickness at pixel i with radius r_i . σ is obtained from fitting the model to the observations of total carbon for $r_i > 0.6 R_p$ [Takahama *et al.*, 2008]. The set of particles reported as spherical is the union of particles meeting this criterion with a set determined to be round by visual inspection.

[14] Nonspherical particles were classified into agglomerations and those containing inclusions and/or films by inspection of intensity images (Figure 1). The observed shape and morphology of a particle may be altered from its

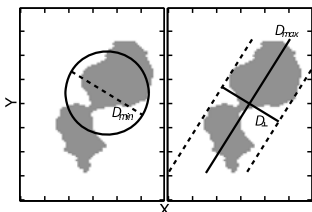
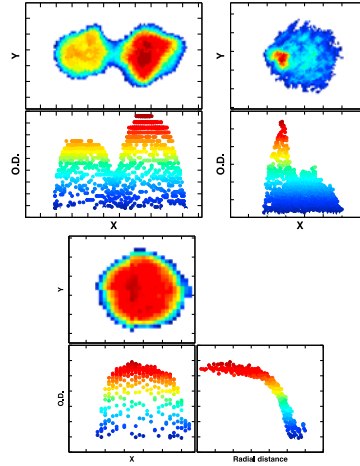
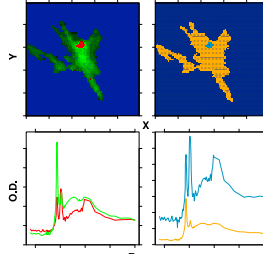
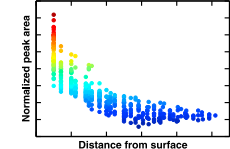
Image Type	Value	Graphic	Description
Binary image	Shape parameters: <ul style="list-style-type: none"> diameter aspect ratio 		Dimensions estimated from binary image
Intensity image	Physical morphology: <ul style="list-style-type: none"> inclusion - regional maxima in intensity agglomeration - aggregation of smaller elements liquid - presence of diffuse film sphericity - radial distribution in greyscale intensity 		From top to bottom: examples of an agglomeration, liquid film and inclusion, and spherical particle are shown. Grayscale intensity images are accompanied by profiles along the elongated direction (mostly meaningful for reflectionally symmetric particles). Image of spherical particle is additionally accompanied by intensity distribution along radial distance from estimated centroid.
Full stack array	Chemical information: <ul style="list-style-type: none"> layers (coatings) inclusions agglomerations 		Factor analysis (PMF; left column) and cluster analysis (right column) decomposes image array into spectroscopically similar regions.
Combined binary and intensity images	Distance information (signal parameterized to distance from boundary)		Integrated R(C=O)OH area is shown to vary as a function of distance from particle boundary.

Figure 1. Summary of methods for investigating particle morphology and heterogeneity.

original state in the atmosphere during the process of impaction onto the silicon nitride substrate during collection, or efflorescence or crystallization following evaporation of water [Mikhailov *et al.*, 2004; Marcolli and Krieger, 2006] in the Helium headspace of the STXM chamber. It is possible that these mechanisms lead to an underestimation of spherical particles and an overestimation in aspect ratios and number of observed agglomerations. Sphericity is not likely to have arisen as an artifact, but may indicate particles existing as amorphous solids, subcooled, or supercooled liquid states [Saathoff *et al.*, 2003; Marcolli *et al.*, 2004]. Cappa *et al.* [2008] observed that nonaqueous-phase organic fraction of atmospheric particle mixtures consisting of a large number of components exhibit liquid-like properties, which is supported by the argument of mutual melting point depression [Marcolli *et al.*, 2004].

2.4.2. Chemical Heterogeneities

[15] We define a chemically heterogeneous particle as one in which its clustered pixel regions are classified into spectroscopically distinct categories (here we use the k -nn algorithm to associate pixel regions to metacategories, as described in section 2.3), or one that we have visually determined to contain variations in chemical composition that are not necessarily captured by the clustering and classification scheme. Existence of such variations are ascertained by examining slices and transformations of optical densities contained in the 3-D $p \times q \times n$ stack array as illustrated in Figure 1. Cluster groups and factor strengths from PMF are mapped back to the spatial domain after analysis to indicate membership or relative composition at each pixel (Figure 1, full stack array row). Classification of spectra for different cluster regions and PMF factors establish

their resemblance to established metacategories [Takahama *et al.*, 2007]. Transformations in spatial coordinate representations (e.g., examination of intensity images and profiles; Figure 1, intensity image row) also aid in determining optical thickness, uniformity and existence of clumps over different regions of the particle. Functional group intensity estimated at each pixel (Table 2) provides an additional method by which spatial correlations among neighboring regions and contrast calculated by texture analysis are evaluated.

2.5. Quantification of Particle Characteristics

2.5.1. Organic Mass Fraction of Dust Particles

[16] For composite particles in which dust and organics are both present, we use PMF and cluster analysis to estimate the mass fraction of organic contained within each particle. PMF can conceptually provide the correct solution, but unconstrained degrees of freedom in the analysis makes it difficult to unambiguously assess the validity of the solution. Cluster analysis is simple and robust, assigning membership in discrete groups, “dust” or “organic,” for each pixel even in the presence of a binary mixture; this method can only provide an approximate answer. Therefore, we use a combination of methods to estimate a value with uncertainties for the organic mass fraction of these particles.

[17] From PMF, the organic mass fraction is calculated as

$$\text{Organic mass fraction} = \frac{M_{org}^{-1} \sum_{i \in \text{Particle}} (n_{org})_i}{M_{org}^{-1} \sum_{i \in \text{Particle}} (n_{org})_i + M_{dust}^{-1} \sum_{i \in \text{Particle}} (n_{dust})_i}, \quad (4)$$

where i is an index indicating pixel, M_{org} and M_{dust} are masses of organic and dust, respectively, per mole of carbon. n_{org} and n_{dust} are moles of carbon in the organic and dust components, respectively, as separated by PMF. The moles of carbon in each component is linearly related to the absorbance attributed to that component (Beer-Lambert Law), so the relevant absorbance from each factor profile (carbon K-edge spectrum) can be substituted into equation (4). The atomic carbon content is related to the edge jump of each K-edge spectrum [Stöhr, 1992], taken to be the difference in absorbance between 320 and 280 eV [Tivanski *et al.*, 2007] (Table 2), so this value is used in place of n_{org} and n_{dust} . From a two-factor solution, the factor profile with greater carbonate to carboxylic carbonyl peak ratio is taken to be the dust component and the other as the organic component.

[18] The organic mass fraction from cluster analysis is similarly calculated as

$$\text{Organic mass fraction} = \frac{M_{org}^{-1} \sum_{i \in S_{org}} n_i}{M_{org}^{-1} \sum_{i \in S_{org}} n_i + M_{dust}^{-1} \sum_{i \in S_{dust}} n_i}. \quad (5)$$

The significant difference between equation (4) is that instead of summing contributions from “pure” organic and dust components, the summation is over the carbon content at each pixel (n_i) with other pixels similarly categorized as either organic or dust (S_{org} and S_{dust} , respectively). The mass to moles of carbon ratio for dust (M_{dust}) in both equations (4)

and (5) is determined by assuming the dust is pure calcium carbonate ($100.1 \text{ g}_{dust}/\text{mole}_C$). A value of M_{org} is assumed to have a value of $20.4 \text{ g}_{org}/\text{mole}_C$, which corresponds to an OM/OC mass ratio of 1.6. This value is in the higher range of OM/OC ratios (where higher values are often assumed for oxidized organic aerosol) measured by Fourier Transform Infrared Spectroscopy [Russell, 2003]. OM/OC mass ratios of common secondary organic aerosol products (e.g., pinonaldehyde, pinonic acid, pinic acid) are close to this value (1.4–1.6). We note that higher values of OM/OC ratios have been reported by analysis of gas chromatography with mass spectrometry and AMS measurements [Turpin and Lim, 2001; Aiken *et al.*, 2008]: 2.1 for ambient aerosols and 2.5 for oxidized components of ambient aerosols from PMF; revised estimates for these cases are discussed in section 3.1.2. Dolomite, another carbonate dust compound has a ratio of $92.2 \text{ g}_{dust}/\text{mole}_C$, so the essential difference between M_{org} and M_{dust} are approximately captured. However, there is a remaining uncertainty in the degree of separation of components or regions which we label as dust or organic; to accommodate this uncertainty we use M'_{org} and M'_{dust} in place of M_{org} and M_{dust} , where the former two variables are defined as a linear combination of the latter two end members,

$$\begin{aligned} M'_{dust} &= \phi M_{dust} + (1 - \phi) M_{org} \\ M'_{org} &= (1 - \phi) M_{dust} + \phi M_{org}, \end{aligned} \quad (6)$$

where ϕ is a value in $[0,1]$ that indicates the degree of separation of the dust component from organic ($\phi = 1$ indicates perfect separation). We use values of $\phi = \{0.8, 1.0\}$ to generate additional solutions to include in our estimate of uncertainty in organic mass fraction.

2.5.2. Layer Thicknesses

[19] Total carbon absorbance of a layered sphere is modeled as

$$\alpha t = \alpha_c t_c + \alpha_o t_o, \quad (7)$$

where t_c is the thickness of the inner core and t_o is the thickness of the outer layer, and α , α_c , and α_o correspond to the absorption coefficient for the sphere, core, and outer layer, respectively. The inner and outer thicknesses can be expressed as a function of the radial distance, r ,

$$\begin{aligned} t_c(r) &= \begin{cases} 2 R_c \sin(\arccos(r/R_c)) & \text{if } r \leq R_c \\ 0 & \text{otherwise} \end{cases} \\ t_o(r) &= t(r) - t_c(r), \end{aligned}$$

where $t(r)$ is the sample thickness of a sphere as a function of radial distance, from equation (2).

[20] Any functional group abundance normalized by total carbon abundance is modeled as

$$\alpha = \alpha_c \gamma + \alpha_o (1 - \gamma), \quad (8)$$

where γ is the ratio of the outer thickness to the thickness of the entire particle; γ can be parameterized as a function of distance from the surface, D [Takahama *et al.*, 2008],

$$\gamma(D) = \begin{cases} \rho^* \frac{\sin(\arccos(1 - D/\rho) \rho^{*-1})}{\sin \arccos(1 - D/\rho)} & \text{if } (1 - D/\rho) \rho^{*-1} \leq 1 \\ 0 & \text{otherwise} \end{cases},$$

Table 3. CCN Surface Tension Parameterizations

Compound	Functional Form	Parameters
Pentanedioic (glutaric) acid ^a	$\sigma'(m_o) = \begin{cases} \sigma_w & \text{if } m_o < m_{o,l} \\ C_0 + C_1 e^{-k(m_o - m_s)} & \text{if } m_o \geq m_{o,l} \end{cases}$	$C_0 = 5.76 \text{ (mN/m)}$ $C_1 = 10.7$ $k = 48.9 \text{ (L/mol)}$ $m_s = 0.125 \text{ (mol/L)}$ $m_{o,l} = 8 \times 10^{-3} \text{ (mol/L)}$ $\sigma_o = C_0 = 57.6 \text{ (mN/m)}$
Octanadecanoic (stearic) acid ^b	$\sigma'(A_o) = \begin{cases} \pi(A_{o,l}) & \text{if } A_o < A_{o,l} \\ \sigma_w - \pi(A_o) & \text{if } A_{o,l} \leq A_o < A_{o,u} \\ \sigma_w & \text{if } A_o \geq A_{o,u} \end{cases}$ $\pi(A_o) = \pi_c + k_B T (A_o - A_s)^{-1}$	$\pi_c = 10.8 \text{ (mN/m)}$ $A_s = 8.37 \text{ (\AA}^2/\text{molec)}$ $A_{o,l} = 15.2 \text{ (\AA}^2/\text{molec)}$ $A_{o,u} = 45.9 \text{ (\AA}^2/\text{molec)}$ $\sigma_o = \sigma'(A_{o,l}) = 24.6 \text{ (mN/m)}$

^aHere m_o is the molality of glutaric acid in water. Parameters for the exponential function is fitted to surface tension measurements by *Varga et al.* [2007].

^b A_o is the area per molecule of stearic acid; k_B is the Boltzmann's constant, and the parameters are fitted to measurements of stearic acid on a water surface by *Donaldson et al.* [2001] for $T = 20^\circ\text{C}$.

where ρ is the radius of curvature of the particle surface, and ρ^* is the ratio of the radius of curvature of the inner surface relative to the particle surface. We approximate the local radius of curvature, ρ , with the projected area sphere radius R_p of the particle. D of any pixel i of the particle is the minimum distance to any background (nonparticle pixel),

$$D_i = \min \{d((x, y)_i, (x, y)_j) : j \in B\},$$

where (x, y) are two-dimensional coordinates of pixel i , d is the Euclidean distance function, and B is the set of background pixels. Particles for which $\alpha_c < \alpha_o$ and the Bayesian Information Criterion (BIC) for this model scored lower than that of the base case model ($\alpha = \mu_\alpha$, a constant value) were considered to have the modeled functional group enriched at the surface.

[21] Equation (7) is appropriate for modeling the absolute absorbance of total carbon in a spherical, layered particle. Equation (8) is appropriate for modeling the variation of a normalized quantity particularly near the surface, and extends to nonspherical particles. The unknown parameters to these equations were estimated from the STXM measurements using linear and nonlinear least squares fitting methods [Bates and Watts, 1988]. For equation (7), the unknown parameters are the core size and total carbon absorbances of the core and outer layer (R_c , α_c , and α_o). After initial fitting, it was found that the interior exhibited negligible absorbance ($\alpha_c \approx 0$) for some particles, so these were refitted with a reduced form of the equation for which only α_o and R_c required estimation. Equation (8) requires the estimation of three nontrivial parameters (ρ^* , α_c , α_o) and were fitted with the full form of the model. Uncertainties for coating thicknesses are calculated from the standard errors of ρ^* .

2.6. CCN Activity Estimation

[22] We calculate the required supersaturation and critical diameter required for a particle of a given composition (surface tension, σ' ; molecular weights of water and solute, M_w and M_i ; dissolved solute mass, m_i ; densities of water and aqueous solution, ρ_w and ρ' ; van't Hoff factor, v_i ; and osmotic coefficient, Φ) to become CCN through a modified Köhler equation [Roberts et al., 2002],

$$S_v^{eq} = \exp \left(\frac{4\sigma' M_w}{k_B T \rho_w D_p} - \frac{\Phi M_w}{\frac{\pi \rho D_p^3}{6} - \sum_i m_i} \left[\sum_i \frac{v_i m_i}{M_i} \right] \right), \quad (9)$$

where S_v^{eq} is the equilibrium saturation ratio, D_p is the droplet diameter, and T is temperature, and k_B is the Boltzmann constant. Glutaric acid and stearic acid are used to represent soluble and insoluble organic acids. These calculations are performed at 20°C . For each of these compounds, partial solubility of components is considered, but Φ and v_i are assumed to be unity. The former decision is reached by assuming that cloud droplets are relatively dilute and behave as ideal solutions. The van't Hoff factor is often empirically determined [Corrigan and Novakov, 1999] but its effective value for glutaric acid has been measured to be around one [Varga et al., 2007] and the unity value for stearic acid is justified by its negligible solubility. *Sorjamaa et al.* [2004] and *Prisle et al.* [2008] suggest the benefits of considering phase partitioning between bulk and surface phases to more accurately model surface tensions (and also vapor pressures) of droplet mixtures. While we do not perform this thermodynamic calculation explicitly, we assume that all stearic acid partitions to the surface, and that glutaric acid coatings are dissolved in the aqueous phase as particles take up water (up to a maximum solubility of 1.6 g/mL; <http://thegoodscentcompany.com>). Furthermore, we parameterize σ' by organic aerosol composition and content, which is fit to surface tension measurements (Table 3). For glutaric acid, an exponential parameterization was fit to surface tension measurements of glutaric acid in water reported by *Varga et al.* [2007]; stearic acid is assumed to be a surface-active, film-forming compound so a van der Waals form of interaction was fit to surface pressure measurements by *Donaldson et al.* [2001]. The resolution provided by the latter parameterization is not strictly necessary but indicates that mass loadings exceeding monolayer thicknesses rapidly approach a value of 25 mN/m, which is in the range of surface tensions measured for pure aliphatic acids (20–40 mN/m) [Jasper, 1972].

3. Results and Discussion

[23] A total of 636 particles were analyzed from the five field campaigns (Figure 2). Particle sizes ranged between 140 nm and 8.4 μm (373 submicron and 263 supermicron; two particles were larger than 10 μm : sampled distribution shown in Figure 3) in projected-area-equivalent diameter; 288 were spherical and 348 were nonspherical. Five meta classes were identified: 173 secondary, 98 biomass burning,

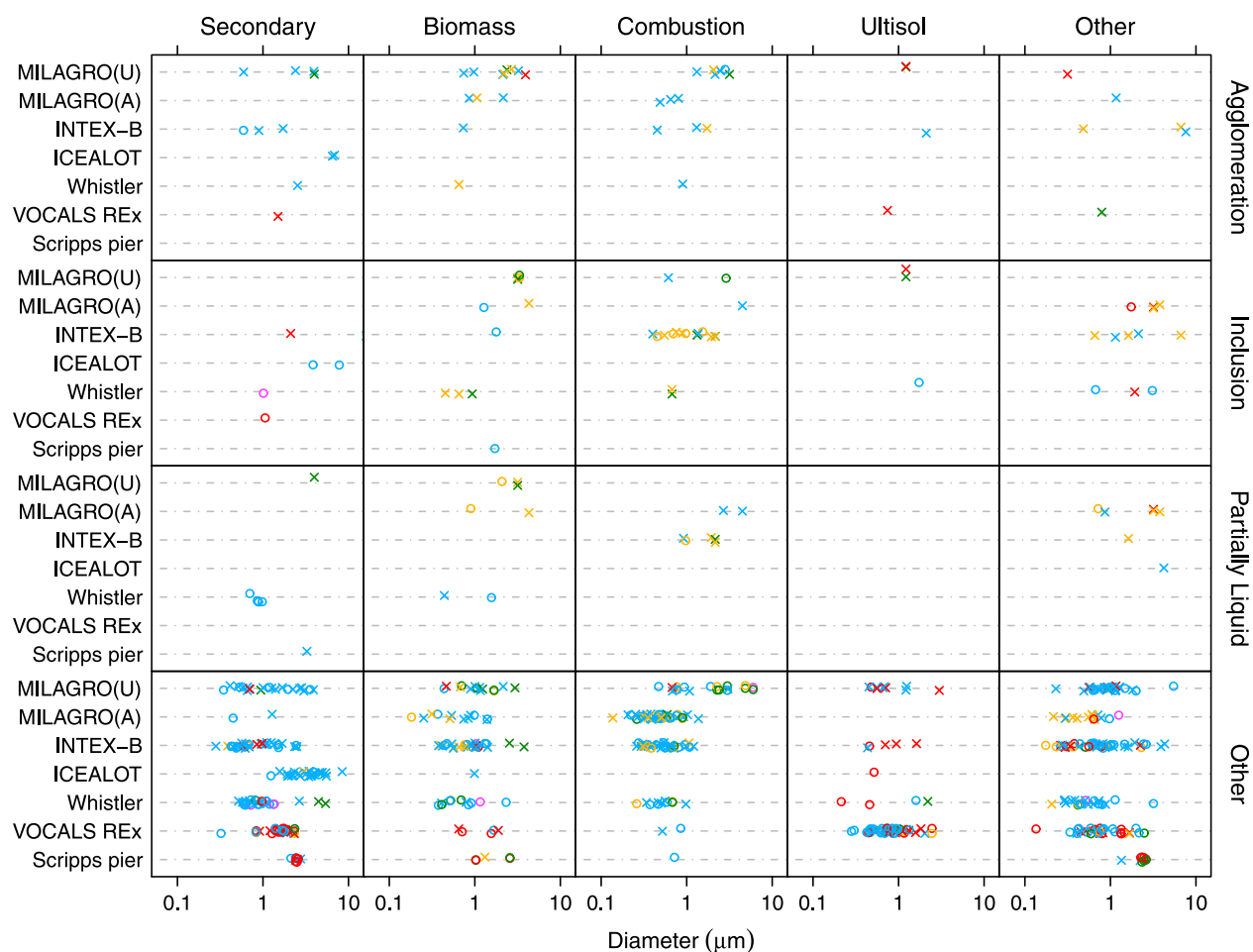


Figure 2. Summary of particles examined. Circles represent spherical particles; crosses represent irregular particles. Colors indicate chemical heterogeneity type: black carbon mixed with soluble material (red; illustration in Figure 5a), organics on dust (dark green; Figure 5b), carboxylic carbonyl enriched at enriched at surface (orange; Figure 5c), inorganic core–organic layer particle (light green; Figure 5d), uncategorized heterogeneous (pink), no heterogeneity detected (blue). Columns represent spectral metaclasses. Rows represent types of morphologies observed. “Other” includes particles for which one of the other three categories did not apply. Some particles may be repeated across plot rows if more than one type of heterogeneity was observed within the same particle. Project abbreviations on left axes are as follows: MILAGRO(U), MILAGRO urban ground site; MILAGRO(A), and MILAGRO aircraft (NCAR C-130).

131 combustion, and 67 ultisol soil, and 166 other. These particles were also characterized by their morphology: agglomerations ($n = 46$), inclusions (45), presence of liquid films (25). Over half of the particles (398) contain some type of heterogeneity; colors in Figure 2 indicate the chemical heterogeneity type and are discussed in more detail in section 3.1.

[24] Extracted aspect ratios for all particles range between 1 and 4.6 (Figure 4). This simple shape descriptor has been used to capture the essential geometry of spheroids for radiative transfer calculations [Hill *et al.*, 1984; Mishchenko *et al.*, 1995, 1997]. Parameters integrated over all scattering angles and orientations (single-scattering albedo, total optical cross section, backscatter fraction) are relatively insensitive to departure from spherical geometry, but the scattering phase function and extinction-to-backscatter ratio can be very different, complicating retrieval of aerosol optical thicknesses from lidar measurements [Mishchenko

et al., 1995, 1997]. For instance, spheroidal geometry in a dust particle population (median aspect ratio of 1.8, ranging between 1.2 and 2.4) imparts a difference of <7% (absolute) on the asymmetry parameter over the spherical case for the range of physically plausible size parameter values. The size parameter is a dimensionless variable proportional to the radius over wavelength of incident radiation and is often used to parameterize optical properties of particles. The asymmetry parameter is an integral of the phase function that characterizes symmetry with respect to scattering: zero for particles with symmetric phase functions, positive for predominantly forward scattering and negative for predominantly backscattering particles. The extinction-to-backscatter ratio is a ratio of integrals of the extinction and backscatter efficiencies; the magnification of extinction-to-backscatter ratio of spheroidal particles compared to that of spherical particles is as much as threefold greater over the

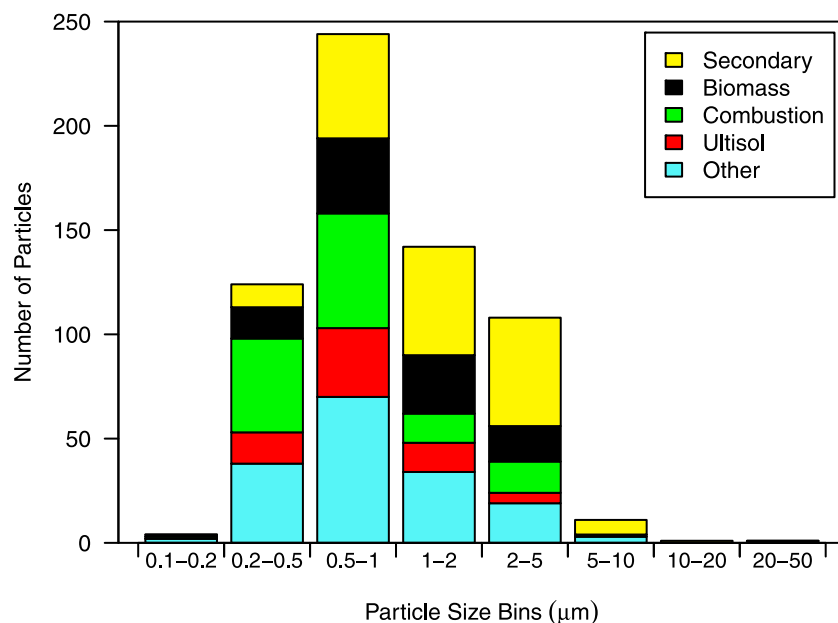


Figure 3. Histogram of analyzed particle sizes.

same range of size parameters (*Mishchenko et al.* [1997], shown in Figure 4).

[25] For our ultisol soil particles, the aspect ratio was $1.3 (\pm 0.3)$, which is smaller than values reported in the literature for dust-like particles [e.g., *Hill et al.*, 1984; *Okada et al.*, 1987], even considering that these are derived from two-dimensional images. This summary statistic is strongly biased by particles collected during the VOCALS

REx campaign, of which more than two thirds (31/44) were classified as spherical (aspect ratio of 1.16 ± 0.16). Aspect ratios for coarse mineral dust have also been calculated from the ratio of the major and minor axis lengths of an ellipse fitted to binary two-dimensional images from electron microscopy [e.g., *Kandler et al.*, 2009; *Coz et al.*, 2009]. Median values of these aspect ratios ranged between 1.6 and 1.81 for dust particles from the Saharan desert, Canary

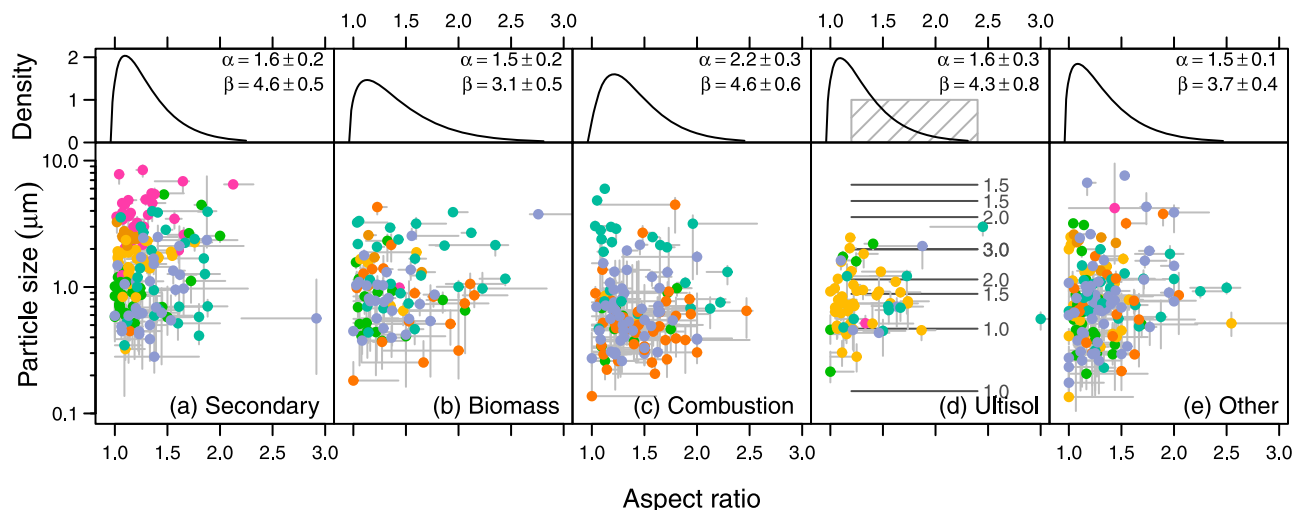


Figure 4. Aspect ratios and particle size by spectra metaclass. Shown above the scatterplots are gamma distribution fits to observed aspect ratios (with an offset of ~ 1), with estimated parameters (shape, α ; scale, β) and their standard errors. Grey shaded rectangle for ultisol densities indicate assumed distribution of aspect ratios for dust by *Mishchenko et al.* [1997]. Points in scatterplot of particle size and aspect ratio are color-coded by project: MILAGRO(U) (teal), MILAGRO(A) (orange), INTEx-B (purple), ICEALOT (red), Whistler (green), VOCALS REx (yellow), and Scripps pier (brown). Four observations with aspect ratio values between 3 and 4.2 are not shown to preserve scale. Horizontal lines in ultisol scatterplot are contours of ratios of spheroidal-to-spherical extinction-to-backscatter ratio at a wavelength of 865 nm for a particle population with aforementioned aspect ratio distribution [*Mishchenko et al.*, 1997].



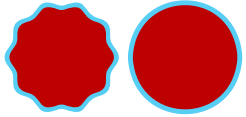

Description	Illustration	Number of particles
a Black carbon with aqueous phase		90 particles
b Organics on dust		106 particles
c Particles surface-enriched in carboxylic acid		23 nonspherical, 31 spherical
d Inorganic core with organic outer layer		10 particles, all spherical

Figure 5. Illustration of categorized particle types.

Islands, Spanish Peninsula, and Puerto Rico [Reid *et al.*, 2003; Kandler *et al.*, 2007; Coz *et al.*, 2009; Kandler *et al.*, 2009]. Our calculations show that using aspect ratios derived by this approach yields slightly higher values than taking the ratios of bounding box dimensions ($y = -0.1 + 1.1x$ with an R^2 of 0.97 for our ultisol particles and $y = -0.2 + 1.2x$ with an R^2 of 0.93 for all particles when regressing our elliptically derived aspect ratios on those estimated by the bounding box method). Kandler *et al.* [2009] report a size (and composition) dependence in aspect ratio for samples collected near the Saharan desert, with smaller particles (<500 nm) having median aspect ratios closer to 1.3. Our elliptically derived median aspect ratio is 1.2 for VOCALS REx, which have a geometric mean diameter of 0.8. Coz *et al.* [2009] additionally suggest that elongated particles may tend to persist during transport, leading to longer aerosol lifetimes for particles with higher aspect ratios.

[26] The mean and standard deviation of aspect ratios for the other types were $1.3(\pm 0.4)$ for secondary, $1.5(\pm 0.4)$ for biomass burning, $1.4(\pm 0.3)$ for combustion, and $1.3(\pm 0.4)$ for other. While freshly emitted particles from combustion are often characterized by fractal parameters, an aspect ratio may also be more appropriate for capturing the geometry of atmospherically processed black carbon particles which are likely to be encapsulated in shells or coatings [Ackerman and Toon, 1981; Fuller *et al.*, 1999; Bond and Bergstrom, 2006; Shi *et al.*, 2008]. The means in aspect ratios were not significantly different across groups, because the ratio varied substantially within each group. No correlation of aspect ratio with diameter, project, or abundance of any single functional group was found for this set of particles.

3.1. Particle Heterogeneities

[27] Four types of heterogeneities are explicitly characterized and discussed in the following sections: black

carbon surrounded by an aqueous phase, organics on dust, particles surface-enriched in carboxylic acid, and inorganic cores encapsulated by an organic outer layer. Each of these types is illustrated in Figure 5.

3.1.1. Strongly Aromatic Carbon Mixed With Aqueous-Phase Components

[28] Ninety particles were characterized by a spatial region with strong aromatic absorbance (corresponding to 285 eV in the NEXAFS spectra) and additional regions containing high absorbances from carboxylic carbonyl (288.7 eV) and potassium (297.4 and 299.9 eV). Five examples are shown in Figure 6. The delineated regions and associated spectra are qualitatively similar between the cluster analysis and PMF results. The strongly aromatic regions are typically identified with black carbon particles and confirmed with k -nn classification into the combustion category [Braun, 2005; Hopkins *et al.*, 2007]. Black carbon components were often observed as an inclusion or at the interior of a layered configuration ($n = 66$) and in agglomerations (8). The 90 particles in this category collectively contained 95 separate regions of strong black-carbon spectral signature associated with the aqueous-phase components (as determined by cluster analysis); 78 were between 0.1 and 1 μm in area-equivalent diameter. The 17 supermicron regions ranged up to 7.5 μm , but these larger instances may be a collection of smaller aggregations that could not be resolved by our pixel resolution (150–300 nm pixel sizes were used in these cases to permit timely data acquisition of >5 μm particles). The observation of supermicron soot aggregates is not entirely surprising, however, as such observations have been reported previously [Kittelson *et al.*, 2000; Johnson *et al.*, 2005].

[29] Combustion processes can often generate particles exhibiting this characteristic of high aromaticity, or sp^2 bonding [Hopkins *et al.*, 2007]. While freshly emitted soot can be described as a fractal agglomeration of spherules, an urban environment can rapidly “age” these particles through condensation of water-soluble compounds [Johnson *et al.*, 2005]. Black carbon particles collected from the atmosphere have been observed in many different types of morphologies: as inclusions in secondary and more soluble species such as ammonium sulfate, or “exclusions” where the soot agglomerates are simply attached to the exterior of the particle bulk [e.g., Katrinak *et al.*, 1992; Adachi and Buseck, 2008]. Katrinak *et al.* [1992] also observed the coexistence of organic and elemental carbon in particles from Phoenix, AZ, using TEM-EELS, and Johnson *et al.* [2005] also suggested that liquid-like coatings on soot observed by SEM/EDX might be organic in composition (lubricating oil or fuel residue).

[30] With the soft X-ray and chemical resolution permitted by the STXM-NEXAFS technique, we are able to observe the presence of potassium and carboxylic acid groups with soot in the same particles. The origins of the acid groups for these particular samples are unclear: Decesari *et al.* [2002] observed formation of polyacids following soot oxidation; the presence of potassium suggests biomass burning sources. Tivanski *et al.* [2007] examined a type of humic-like particles from biomass burning events. Combustion smoke from such events can also generate black carbon particles with significant impacts on climate [Crutzen and Andreae, 1990]. The composition of the surrounding medium in our samples suggests that these black carbon particles are encapsulated

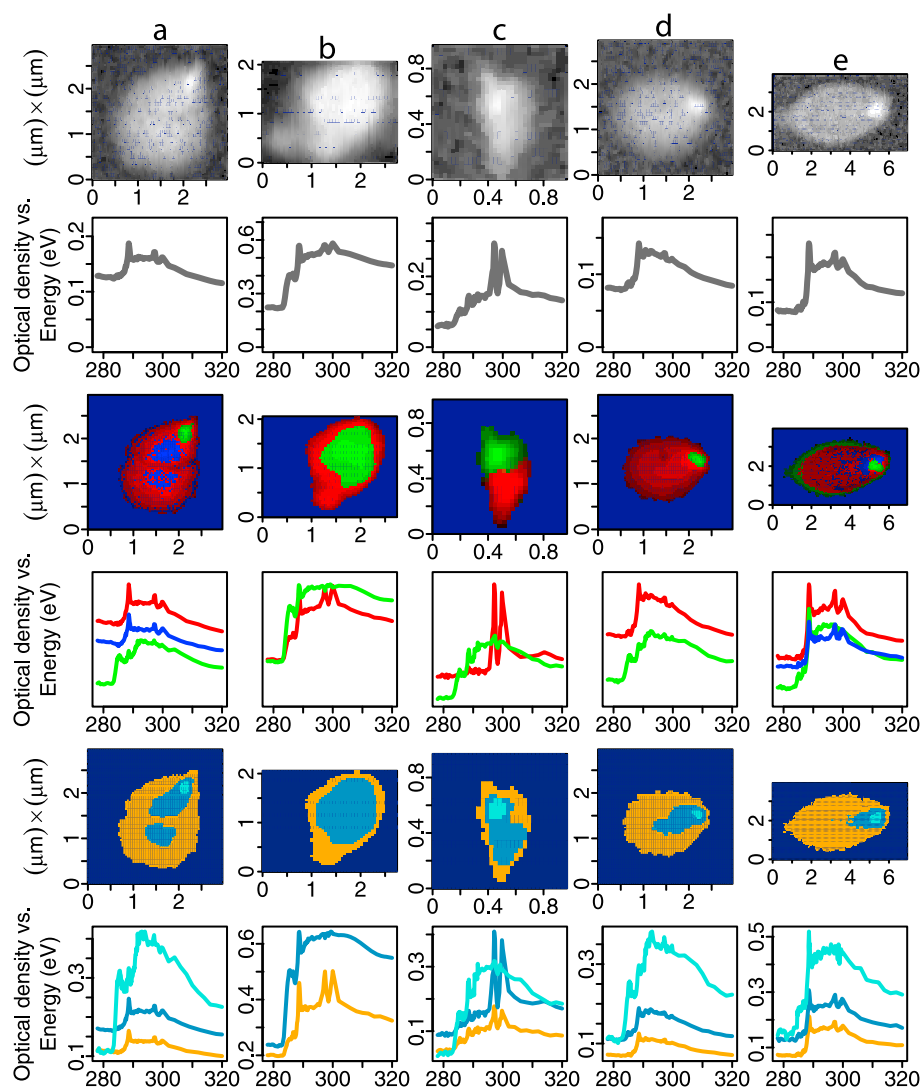


Figure 6. Examples of aromatic carbon and soluble material. Each column contains information regarding an individual particle. (a) Particle from MILAGRO (urban ground site); (b) particle from MILAGRO (aircraft); and (c, d, and e) particles from INTEx-B. (top to bottom) Images of total absorbance (white indicates higher value); average spectra; images of factor analysis component contributions (ranging along red-green or red-green-blue coordinates for first and second and first through third components, respectively); component profiles from factor analysis; images of particle regions grouped by spectral similarity from cluster analysis; and average spectra for each region in the previous row.

by a single phase that includes carboxylic acids and potassium. Given the solubilities of many carboxylic acid compounds and potassium salts in water (CRC Handbook of Chemistry and Physics, 89th edition, <http://www.hbcpnetbase.com>), a common aqueous phase is a likely medium in which these compounds are dissolved. The enhancement in absorption of radiation by black carbon particles when coated with non-absorbing species have been reported in the past [Bond and Bergstrom, 2006]. Such coatings can increase the absorptivity of black carbon particles on average by a factor of ~ 1.5 (calculated as the average between aggregated soot particles and soot aggregates coated with layers approximately four times the core volume [Bond et al., 2006]) and increase the predicted radiative forcing due to black carbon by twofold globally when contrasted with the assumption that black

carbon exists as an external mixture with scattering species [Jacobson, 2001]. Hygroscopic coatings can also increase the wet removal rates of black carbon particles [Zuberi et al., 2005], further highlighting the importance of observing the degree to which black carbon is mixed with other compounds.

3.1.2. Organics and Dust

[31] Both cluster analysis and PMF revealed variations in the proportions of carbonate and carboxylic acid groups within the same particle in 106 cases; a few examples are illustrated in Figure 7. The results of the PMF analysis illustrated suggest that the two components, separated by relative absorbances of carbonate and carboxylic carbonyl, often appeared in clumps, approximately coincident with cluster groupings, rather than uniform coatings of one on

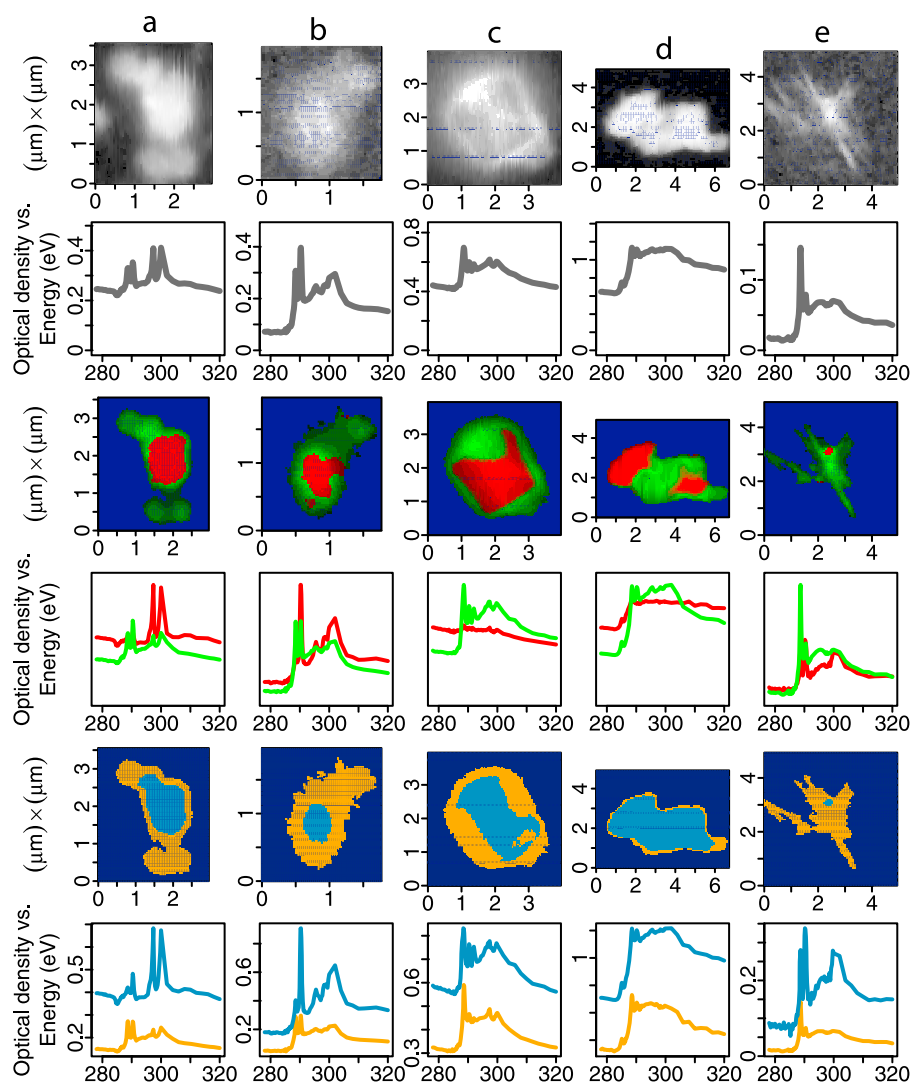


Figure 7. Examples of dust and organic particles. Layout is the same as in Figure 6. Particles in Figures 7a and 7e are from INTEX-B; particles in Figures 7b–7d are from MILAGRO (urban ground site).

the other (which would otherwise be indicated by significant differentiation in component contribution near the particle edges). Pine utlisol soil spectra reported in the literature exhibits strong absorbance by carboxylic carbonyl (288.7 eV), carbonate (290.4 eV), and potassium regions (297.4 and 299.9 eV). We have previously associated spectral similarity to this reference type (with the defining feature being the presence of a carbonate peak) as an indication of dust-like composition with possible contributions from organic material having condensed during transport [Leaitch *et al.*, 2009]. While cooccurrence of organic and dust signatures suggests condensation or coagulation except for the case of a common organic dust source, the component spectra containing less of the carbonate peak often exhibits a strong carboxylic carbonyl feature that asymptotically approaches the secondary-type spectra found in a large number of atmospheric particles [Takahama *et al.*, 2007]. Therefore, it is possible that these particle spectra comprise varying contributions of the secondary-type spectra and dust-like spectra (characterized by a strong carbonate signature). This interpretation is consistent with the findings

of Sullivan and Prather [2007], who found that oxalic and malonic acids, common secondary organic aerosol constituents, were often internally mixed with mineral dust particles during the ACE-Asia campaign. The proposed mechanism is the “rapid photochemical oxidation of gas-phase precursors followed by condensation near source emissions” [Sullivan and Prather, 2007], which is likely to be an active pathway in other geographical regions. Quantification of the organic mass fraction relative to dust based on carbon content of spectra segregated by factor and cluster analysis reveals a wide range of values (Figure 8a). Having considered a range of uncertainties including the method of spectra attribution and quality of separation between organic and dust-like spectra (section 2.5), we estimate the organic mass fraction for these particles to be $0.3 (\pm 0.2 \text{ standard deviation})$ on average. If a higher value of OM/OC is assumed (2.5 [Aiken *et al.*, 2008] rather than 1.6) a 16% ($\pm 4\%$ standard deviation) relative increase in organic mass fraction is estimated, raising the average organic mass fraction of these particles to $0.4 (\pm 0.2 \text{ standard deviation})$. For both calculations, the median values for our samples

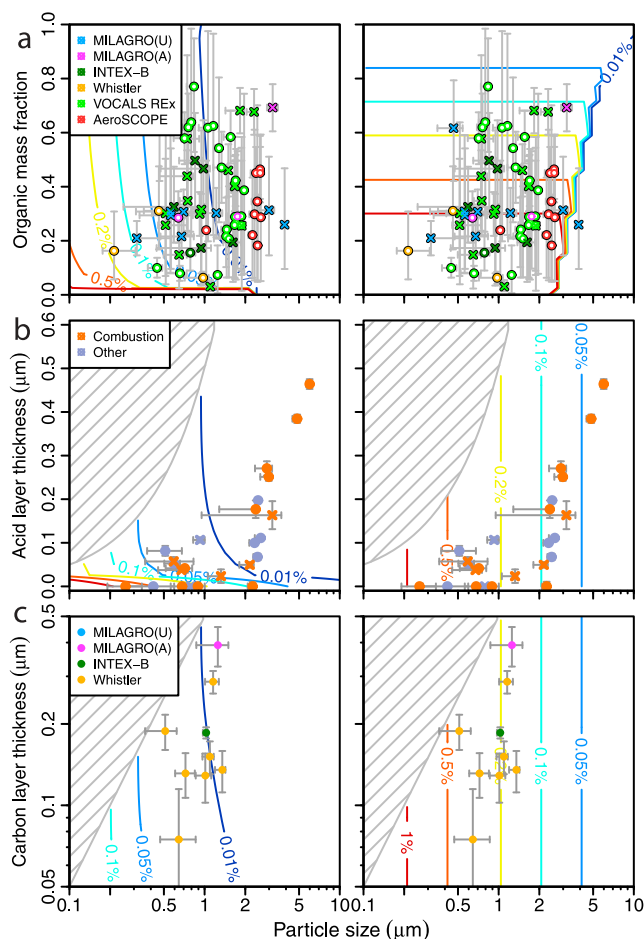


Figure 8. Mass fractions, coating thicknesses, and particle size measurements superposed on lines of critical supersaturation. Left and right plots differ by assumed composition of organic component: (left) glutaric acid is used to represent organic mass, and (right) stearic acid represents the organic fraction. (a) Estimated fraction of organic mass on calcium carbonate dust (particle type in Figure 5b, for particles collected on 19 separate STXM windows). Error bars represent range of estimates from PMF and cluster analysis with values of ϕ (equation (6)) of 0.8 and 1.0. Points represent the mean of these values. Circles represent spherical particles, and crosses represent irregular particles. Supersaturations are calculated for organic compounds on calcium carbonate. (b) Thickness of carboxylic carbonyl coating on particles classified as combustion or other (subset of type illustrated in Figure 5c); circles represent spherical particles, and crosses represent irregular particles. Supersaturations are calculated for organic compounds on black carbon (insoluble cores). (c) Thickness of carbon coatings (all particles are spherical) on inorganic cores (Figure 5d). Supersaturations are calculated for organic compounds on quartz (insoluble cores). A single particle with a size of 5 μm and coating thickness of 2 μm was omitted for considerations of scale. Grey shaded regions indicate regions where layer thicknesses exceed particle sizes (unfeasible region).

were below 0.5 (0.30 and 0.37). While dust particles are generally considered to be nonspherical, over half (57) of the dust particles we examined were classified as spherical, particularly those collected during the VOCALS REX campaign (34 out of the 57 spherical dust particles were from this campaign). This observation may be attributed to the presence of organic compounds (particularly those containing carboxylic acid functional groups, which are polar and hygroscopic), increasing the propensity for water uptake and dissolution of the carbonate minerals, though the possible influence of other hygroscopic species cannot be ruled out.

[32] While *Bauer et al.* [2007] assumed that liquid refractive material uniformly coats dust particles, our results show that the organic compounds cooccurring with dust in dry conditions in the STXM chamber are not necessarily found as coatings. In addition to the impact on direct radiative forcing, the net effect of mixing of organics and dust on the energy balance should be considered, as the dust may become more CCN active as a result of this type of processing, but also susceptible to wet removal. Furthermore, the mass and number of externally mixed organic aerosols may also decrease when condensation surfaces are provided by dust aerosols, leading to a reduction in forcing from the former population. Such a scenario was outlined and tested by computer simulation for sulfate formation on mineral dust surfaces [*Bauer and Koch, 2005*], and observations of organic groups condensed on dust particles share many possible implications. We examine one aspect of these possible changes with Köhler theory calculations (equation (9)). Figure 8a shows critical supersaturations required for observed dust particles (assumed to be calcite) to become CCN when the organic fraction is assumed to have the properties of glutaric acid (Figure 8, left) and stearic acid (Figure 8, right) to contrast two extremes of solubility. If the organic fraction is assumed to be as hygroscopic as glutaric acid, all of the particles reported here would activate at 0.2% supersaturation (Figure 8a, left). As typical cloud supersaturations in the marine boundary layer lie between 0.1 ~ 0.3% [*Baker and Charlson, 1990; Hoppel et al., 1996; O'Dowd et al., 1997*], sensitivity of critical supersaturations in this domain are of particular interest. If the organic fraction was insoluble like stearic acid, however, the particles would not activate unless the dust particles were large ($>2 \mu\text{m}$) or largely organic (Figure 8a, right). Unactivated dust aerosols have been shown to act as ice nuclei [*DeMott et al., 2003*], and the increase in hygroscopicity of dust aerosol by organic compounds may reduce their behavior in this role.

3.1.3. Surface Enrichment of Carboxylic Carbonyl

[33] Fifty-four instances of significant surface enrichment of carboxylic carbonyl were found: 31 in spherical and 23 in nonspherical particles. Examples for the spherical case are shown in Figure 9, with significant enhancement in normalized (relative to total carbon) carboxylic carbonyl abundance observed toward the particle surface. Six of these particles were classified as secondary, 18 as biomass, 15 as combustion, six as ultisol, and 9 as other. Coating thicknesses of carboxylic acid estimated by our simple layered particle model (equation (8)) ranged between $<30 \text{ nm}$ and 0.6 μm (<1 to 53% of the particle radius; Figure 10). For particles with estimated coating thicknesses less than the

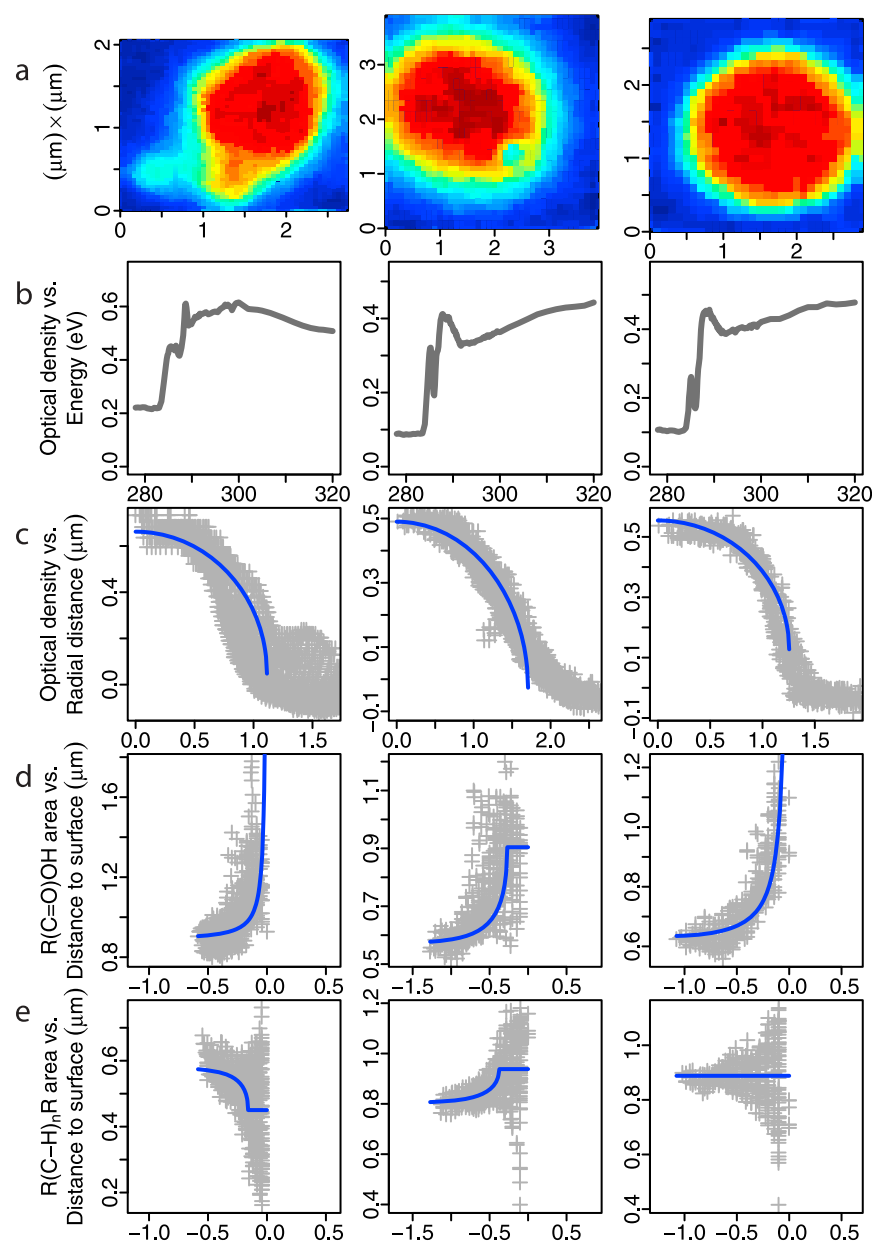


Figure 9. Surface enrichment of carboxylic carbonyl groups. Each column contains information regarding an individual particle. Particles in all columns are from MILAGRO (urban ground site). (a) Images of intensity at 288.85 eV (red indicates higher value); (b) average spectra; (c) intensity at 288.85 eV as a function of radial distance (line indicates model for spherical particle fitted to the data); (d) carboxylic acid $[R(C=O)OH]$ peak area normalized by total carbon absorbance as a function of distance to particle boundary with layered particle model fit as blue line; and (e) same as Figure 9d but with normalized alkyl $[R(C-H)_nR]$ group peak area.

image pixel resolution (<30 nm), it is possible that the coating thicknesses may be even finer than reported (with significantly higher carboxylic carbonyl groups concentrated at the surface) as residual deviance asymptotically decreases with smaller coating thicknesses due to limits in numerical fitting. At the other extreme, several estimated coating thickness were quite large (>100 nm) and suggests that the acid coatings in these particles would extend beyond several monolayers.

[34] The layered particle model (equation (8)) was similarly fitted to the integrated alkyl absorbance profile (as a

function of distance from particle surface). While these estimated coating thicknesses for alkyl groups correlate with thickness values estimated from the carboxylic carbonyl profiles (Pearson's $r = 0.8$), the abundance of alkyl groups did not always increase, as observed for the acid groups. In 29 of the cases (2 secondary, 8 biomass, 10 combustion, 5 ultisol, and 4 other), the alkyl group abundance showed an increase at the surface layer; in 17 cases (2 secondary, 8 biomass, 2 combustion, 1 ultisol, and 4 other) there was a decrease; and in 4 cases (3 combustion and one other type), the alkyl group abundance across the particle profile was best

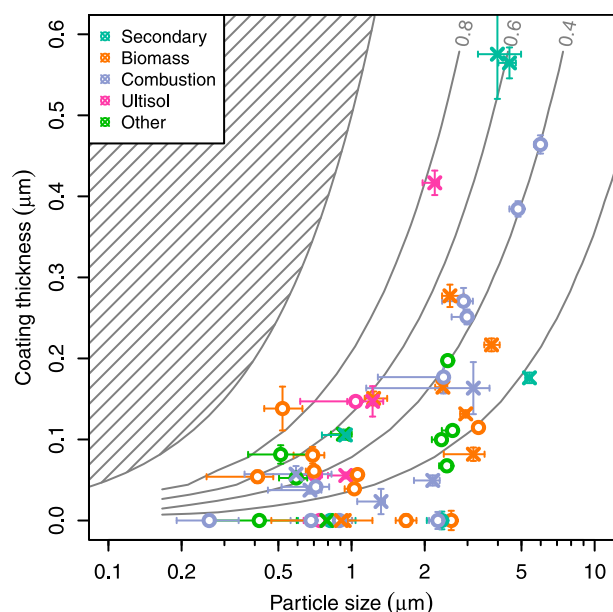


Figure 10. Thickness of carboxylic carbonyl coatings on layered particles. Particles shown here belong to the superset containing those in Figure 8b (right). Grey hatched regions indicate regions where layer thicknesses exceed particle sizes. Grey contour lines indicate volume fraction {0.2, 0.4, 0.6, 0.8}.

represented with a constant value. Figure 9 shows examples of each of these cases along with the model fitted to the acid group profiles.

[35] Observations of surface-active organic compounds in atmospheric particles have been reported previously [e.g., Russell *et al.*, 2002; Tervahattu *et al.*, 2002a, 2002b, 2005]. While the acids observed by Tervahattu *et al.* [2002a, 2002b, 2005] in marine and continental environments commonly ranged between 10 and 30 carbon atoms in size, Minofar *et al.* [2004] systematically studied the effect of carbon chain length on the surface activity of functionalized organic compounds by molecular dynamics simulation and reported that diacids with as little as eight carbon atoms can be preferentially solvated at the surface of an aqueous solution. Our observation of the three cases of abundance (enriched, decreased, and unchanged) of alkyl groups at the surface accompanying surface enrichment of carboxylic acid groups suggests that a wide variety of organic molecules can indeed form organic coatings on particle surfaces in the atmosphere. Those cases in which the alkyl groups are enriched at the surface along with the acid groups may indicate the presence of long-chain fatty acids, while those with decreasing alkyl abundance accompanying increasing abundance of acids may suggest the presence of smaller, more fragmented molecules relative to those found in the interior of the particle.

[36] There are numerous implications for these organic coatings or films on atmospheric processes. Shilling *et al.* [2007] found that the production of a few percent (by mass) of surface-active species (oxidation products of α -acyloxyalkylhydroperoxide and oleic acid) lowered critical supersaturations by nearly 0.5%. Such a small change in mass cannot alter hygroscopicity to explain the observed

difference in critical supersaturation, so a lowering of surface tension by surface-active species was hypothesized and supported by Köhler theory calculations. Kuwata *et al.* [2007] additionally found that the CCN activity of black carbon particles in Tokyo were positively correlated with thicknesses of coatings (on the order of <10 nm) elucidated by a volatility tandem differential mobility analyzer (with an operation temperature of 400°C). Dusek *et al.* [2006] reported that even a coating of 5% (by weight) of sodium chloride decreased the critical supersaturation of black carbon particles (approximately 150–400 nm in diameter) by 0.3% over the case in which there was no coating; hydrophilic organic coatings can similarly increase CCN efficiency of black carbon particles. Hings *et al.* [2008] report such findings for soot particles coated with glutaric acid, for particles between 80 and 250 nm with coating thicknesses in the range between 10 and 50% of the particle diameter. We also illustrate this sensitivity of CCN activity to coating thickness by superposing lines of critical supersaturation on acid-coated combustion-type (and other type) particles that we observed (Figure 8b, left). Coatings as thin as 30 nm can significantly alter the required critical supersaturation for these particles, as evidenced by steep gradients in the %-supersaturation surface. If the coating compound is insoluble (represented by stearic acid in our example), the coating has negligible influence and the particle size becomes the primary variable controlling CCN activity for the sizes and coating thicknesses reported here (Figure 8b, right). In addition to influencing particle solubility, hydrophobic organic coatings can suppress CCN activation of an insoluble particle by reducing the wettability of the surface [Dusek *et al.*, 2006].

[37] We note here that the total number of CCN is dependent upon the cloud-activated fraction times number concentration. The activated fraction depends on the size and chemistry of the particles [Roberts *et al.*, 2002; Dusek *et al.*, 2006], and the number concentration is a function of emission or formation and removal. While many of the particles we have examined are likely to become CCN in the presence of soluble organic material, these particles also fall into the larger range of accumulation mode or the tail of the coarse-mode particle distribution [Seinfeld and Pandis, 2006], and have increasingly large deposition dry velocities and likelihood for removal by scavenging [Seinfeld and Pandis, 2006] relative to particles at the peak of the accumulation mode (<500 nm). Addition of coatings such as those we have reported here on smaller particles will have an even greater effect on particles, becoming CCN (as illustrated by contour gradients in Figure 8b).

[38] With regards to kinetic effects of coatings, Chakraborty and Zachariah [2008] simulated hydrophobic organic compound surrogates coating a 4 nm aqueous droplet and found that such coatings can reduce sticking probabilities of water vapor to particles 11–16% with respect to unity mass coefficients for vapor molecules impinging on a pure aqueous droplet. Chakraborty and Zachariah [2007, 2008] additionally found that such organic films can also increase overall particle water uptake, contrary to previous conceptions; the driving force for this phenomena was explained by the reduction in energy associated with maintaining curvature in the film. While these conclusions are relevant for small droplets coated by a monolayer of fatty acid, the effect of

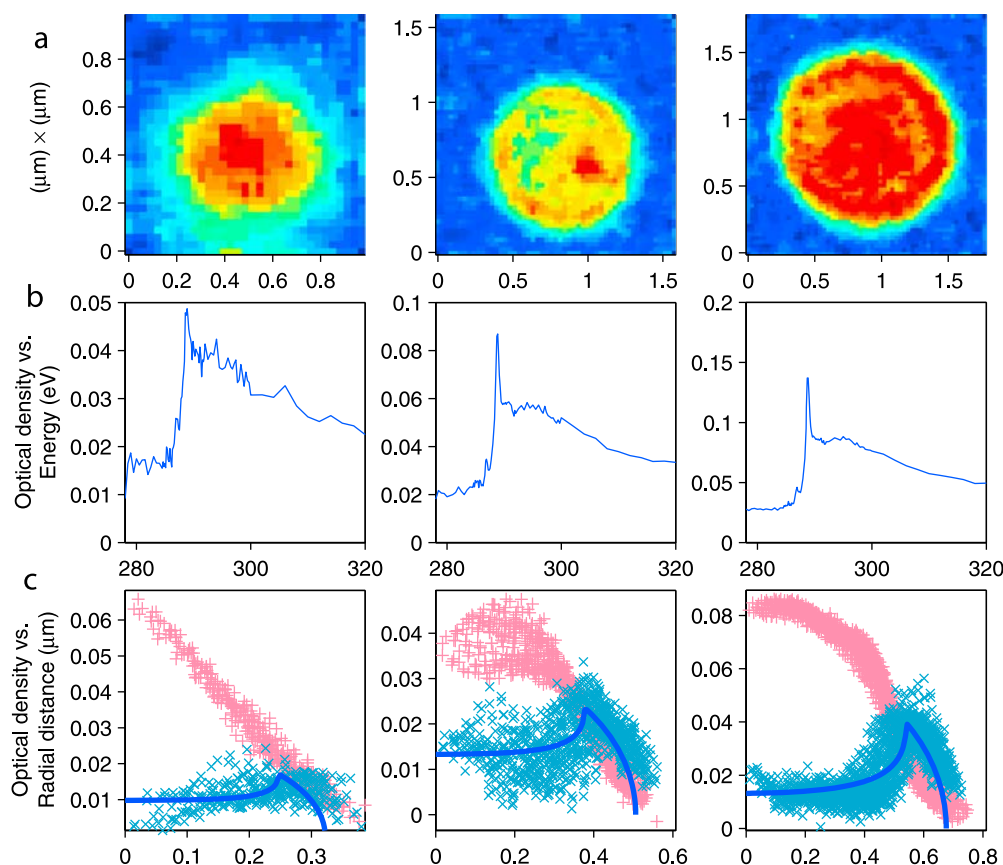


Figure 11. Examples of inorganic core–organic coating types. Each column contains information regarding an individual particle. All particles are from the Whistler campaign. (a) Images of intensity at 288.85 eV (red indicates higher value); (b) average spectra; and (c) intensity at 288.85 eV as a function of radial distance (pink pluses indicates preedge absorbance, and blue crosses represent total carbon absorbance; blue line is fit to total carbon absorbance).

thicker coatings and larger particles is relatively unknown. *Chuang et al.* [1997] report that cloud-droplet growth kinetics becomes especially sensitive for mass accommodation below 0.1, and [Feingold and Chuang, 2002; Medina and Nenes, 2004] found that organic films may cause sufficient retardation in water uptake dynamics to alter cloud droplet distributions even if equilibrium water uptake is unchanged.

3.1.4. Inorganic Cores With Organic Coatings

[39] Ten particles with predominantly inorganic cores and organic shells were found (examples in Figure 11). Seven of these particles were collected in Whistler; INTEX-B, MILAGRO (urban ground site), and MILAGRO (aircraft) each contributed an additional member to this set. Nine of the particles ranged in diameter between 0.8 and 1.7 μm , with one particle having a diameter of 6.2 μm . The diameter of the core varied between 30 and 80% ($60 \pm 20\%$ mean and standard deviation) of the particle diameter (Figure 8c). Though the overall spectra types were categorized as secondary by the classification algorithm for their prominent carboxylic carbonyl absorbance, carboxylic carbonyl absorbance normalized by carbon thickness indicated no significant variation over the core or coating, except for the case of a single particle that was jointly categorized as having an inorganic core and surface enrichment of carboxylic carbonyl. The relative uniformity of the organic

composition over the particle as suggested by the spectra can be explained with an oxidation-condensation or volume-limited oxidation mechanism. A notable difference is observed, however, in the integrated values of total carbon and preedge absorbance (Figure 11c). Estimating parameters of core size and absorption of carbon for a spherical particle (equation (7)) gives an indication that in six of these 10 particles, the contribution of the inner core to carbon absorption was negligible. In the remaining four, the absorption of the core relative to the outer layer was between 15 and 30% with one at 70%. The outer layer is not entirely carbon, however, as densities calculated assuming pure carbon yield unrealistic values ($<0.05 \mu\text{g}/\text{m}^3$ or g/cc).

[40] The apparent sphericity implies that these particles may be retaining an aqueous phase at low relative humidity, or existing as a supercooled or subcooled organic phase, consistent with the observations by *Saathoff et al.* [2003] and *Cappa et al.* [2008] for laboratory-generated secondary organic aerosol or multicomponent organic mixtures. The preedge absorbance is due to absorbance contributions from a number of possible elements associated with inorganic compounds in the particle. Silicon and sulfur have high photoabsorption cross sections at 280 eV (5.0 and $4.0 \times 10^4 \text{ cm}^2/\text{g}$, respectively; Center for X-Ray Optics, <http://www-cxro.lbl.gov>) which make silicate dust and sulfates possible candidates for cores. The significance of a phase separation,

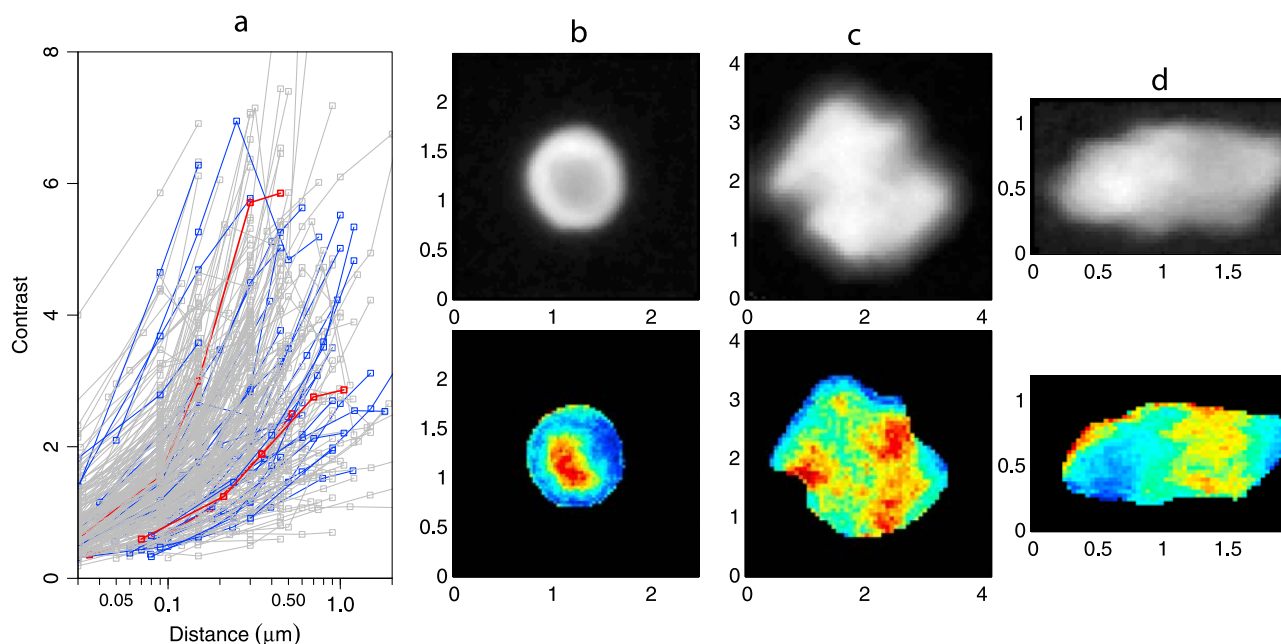


Figure 12. Variation of carboxylic carbonyl abundance normalized by total carbon as a function of distance between pixels. (a) Variation in contrast parameter, a measure of the correlation in intensity among pixels separated by the indicated distance, with pixel separation distance converted to micrometers. Squares represent distances corresponding to separation by 1, 3, 5, 10, and 15 pixel units. Contrasts for separation distances less than the radius of the particle are not shown. Each line corresponds to a separate particle; blue line represents particles in the surface-enriched carboxylic group category, and red lines correspond to contrasts for the three particles shown. Example images are given for individual particles (units are in μm): (b) particle from MILAGRO (urban ground site) and (c and d) particles from INTEx-B. Figures 12b–12d (top) show the total carbon intensity (white indicates more carbon); Figures 12b–12d (bottom) show normalized intensities of integrated carboxylic carbonyl abundance (red indicates higher value).

between core and outer layer in this case, is notable for purposes of calculating CCN potential and optical depth. For instance, modifications to Köhler theory permits prediction of CCN activity parameterized on soluble/insoluble fraction; Roberts *et al.* [2002] found that for conditions observed in the Amazonian tropics the cloud droplet formation was extremely sensitive to this parameter. Kelly *et al.* [2007] also found that quartz (SiO_2) cores coated with soluble material (5–25 nm) increased their CCN activity. Carboxylic acid coatings observed in our particles can increase CCN activity over that of a pure, insoluble core material both by altering the soluble fraction and also increasing the particle size. Figure 8c illustrates an example where quartz is coated by either glutaric acid (Figure 8c, left) or stearic acid (Figure 8c, right), to represent soluble and insoluble organic components. If the solubility of the organic fraction approaches that of glutaric acid, all of the particles reported here would be likely to activate as their required supersaturations are reduced below 0.1% (if no coatings existed on the quartz cores, required supersaturations for the submicron particles would exceed 0.3%). If the organic fraction is insoluble, it will increase the likelihood for the quartz particle to become CCN through simple volume addition to the particle (assuming a wettable surface (illustrated in Figure 8c, right). In the case that the core is hygroscopic (e.g., comprising sulfate(s)) and the coating is an insoluble fatty acid, for instance, the CCN activity can

conversely be decreased or act as an inert mass [Cruz and Pandis, 1998]. According to our calculations, ammonium sulfate particles with these core sizes and insoluble coatings will still activate at supersaturations less than 0.1%, due to the hygroscopicity of ammonium sulfate. For calculations of light scattering, these particles represent a case of symmetric, layered particles, which behave different optically than volume mixtures of the same average composition [Mishchenko *et al.*, 2002; Bond *et al.*, 2006].

3.1.5. Spatial Distribution of Functional Groups From Texture Analysis

[41] Carboxylic carbonyl was distributed nonuniformly for particles enriched in this group at the surface, but also for other particles in which the surface enrichment of carboxylic groups was not explicitly detected. Figure 12 shows three example images in which nonrandom variability in normalized carboxylic carbonyl abundance is observed over the particle. An analysis of a contrast parameter derived from an intensity cooccurrence matrix generalizes this observation to show that this spatial correlation is observed in many instances (Figure 12a). While this correlation may be partially enhanced by limitations in focus and resolution in this analysis, the contrast for an intensity image lacking any spatial dependence should remain relatively fixed at larger pixel separation distances for each particle. One additional artifact may arise from the increasing symmetric errors in quantified intensity toward optically thin regions (near

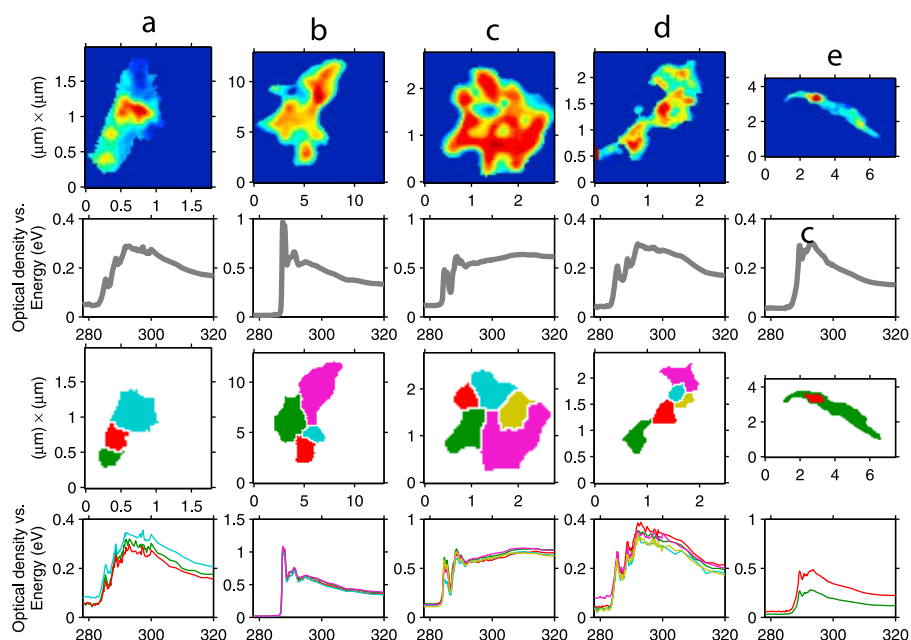


Figure 13. Spectroscopic differences among regions in unclassified agglomerations and inclusions. Each column contains information regarding an individual particle: (a) from MILAGRO (aircraft), (c and d) from MILAGRO (urban ground site), and (b and e) from INTEx-B. (top to bottom) Total carbon absorbance (red indicates higher value), average spectra, image segmented by watershed transform [Gonzalez *et al.*, 2003] or *h*-dome extraction [Vincent, 1993], and spectra according to regions defined in the previous row.

particle boundaries), but examination of individual images suggests that the increase in contrast arises in most cases from having a nonuniform distribution in intensity over increasing spatial scales, rather than from boundary effects.

[42] In a study of oleic acid vapor deposition onto $1.6\ \mu\text{m}$ polystyrene and silica particles, Garland *et al.* [2008] observed islands of oleic acid with size dimensions of approximately 100 nm forming instead of uniform coatings. Chakraborty and Zachariah [2008] observed, by simulation, aggregation of fatty acids on regions of a water nanodroplet (approximately 4 nm in diameter), with the explanation that this structure reduces local surface curvature. While surface energy contribution to morphology and configuration is likely to be negligible in the larger particles studied by our method, Moussa *et al.* [2009] observed the uniformity of molecular coverage on a flat surface depends on the strength of interaction between surface and coating material (water on self-assembled monolayers, in this case). The heterogeneous distribution observed in our particles may be a combination of nonuniform surface coverage and also internal (volumetric) variation in compound distribution, which may be enhanced by drying effects. A nonuniform surface coverage of carboxylic acid will affect predictions of mass transfer and CCN activity from the perspective of exposed surface area for molecular exchange [e.g., Bahadur and Russell, 2008; Chakraborty and Zachariah, 2008]. As such, existence of heterogeneous surfaces may require reconsideration of mass accommodation coefficients for vapor molecules condensing onto mixture surfaces and surface tensions for calculating CCN potential of aerosols, if they are to be derived from mechanistic models. Internal heterogeneities, particularly in the extreme case of phase

separation, can generate deviations from expected component mole fractions used to calculate activity coefficients, vapor pressures of multicomponent mixtures and aerosol optical properties [Kocifaj *et al.*, 2006].

3.2. Unclassified Heterogeneities

[43] Liquid films identified ($n = 25$) by intensity profiles (Figure 1) were often associated with strong potassium or carboxylic carbonyl absorbances, consistent with our understanding of the relatively high solubility of these species. Two examples are shown in Figures 6d and 6e. These particle images consist of an inclusion and liquid region. Spectra from the liquid region show strong absorbances in the carboxylic and potassium. Often, the liquid films analyzed in this study were surrounding inclusions, but this may be an instance of biased selection as inclusions and regions surrounding them are more likely to be selected (regions of sample substrates with high carbon optical density are targeted) for analysis.

[44] There were 32 particles characterized as having an agglomeration or inclusion-type morphology for which discrete types were not defined, and 131 additional heterogeneities were detected by examination of clustered pixel spectra but not categorized. In the former case, chemical differences as interpreted from the spectra were not resolvable by our method. In the latter case, the spectra varied only marginally, were unique, or not amenable for physically meaningful descriptions. Figure 13 shows five particles not belonging in any of the categories discussed in sections 3.1.1–3.1.4. Comparison of average spectra over individual regions indicate subtle differences, such as contrast in the aromatic absorbance (Figure 13c), total carbon to

preedge ratio (indicative of organic/inorganic ratio; Figure 13d), or indiscernible difference in spectra (Figures 13a, 13b, and 13e). The occurrence of nonspherical morphologies and heterogeneities is not surprising, as the number of chemical compounds in the atmosphere are large (e.g., *Hamilton et al.*, 2004) and combine in the condensed phase through a large number of atmospheric processing mechanisms: emission, reaction, condensation or evaporation, and coagulation and scavenging [Seinfeld and Pandis, 2006]. One limitation to full characterization of more types by carbon K-edge analysis is that elements excluded by this X-ray energy window are not explicitly characterized. Agglomerations or inclusions with no apparent spectroscopic differences across each particle may represent mixtures of miscible but chemically distinct components.

4. Conclusions

[45] We used carbon K-edge spectromicroscopy to characterize physical and chemical attributes for 636 particles collected during six field campaigns. The measured distribution of aspect ratios of dust and other particles in our samples ranged nonuniformly between 1.0 and 4.6 with a mean of 1.4, which can affect aerosol optical retrieval over the case in which spherical geometry is assumed. These shapes did not show any correlations with spectral signature (meta category), size, or geographical location in which the particle was sampled. One type of chemical heterogeneity observed was black carbon particles covered by carboxylic acid and potassium in a single phase ($n = 90$). The acid and potassium were collocated in an aqueous phase, in some instances as a liquid film on the substrate with the black carbon particle existing as an insoluble inclusion. Seventy-eight of the black carbon regions found within these particles were submicron in size. Dust particles with organic clumps were also observed ($n = 106$), with organic mass fractions estimated to be less than 0.5 on average. These particles presumably originated as dust and were transformed through condensation of and coagulation with organic aerosol, which may affect their removal rates and the magnitude of their participation in radiative forcing. Particles enriched in carboxylic acid at the surface ($n = 54$) were observed among different meta types and shapes, with coating thicknesses estimated to be <30 nm to 600 nm. Köhler theory calculations show that soluble coatings (e.g., glutaric acid) of this thickness on black carbon cores can reduce the critical supersaturation of these particles by as much as 0.1%. Inorganic cores with organic coatings were also observed ($n = 10$); these particles were spherical and the organic fractions were classified as secondary due to the prominent carboxylic carbonyl feature in their spectra. The organic carbon layer was in general thicker (70 nm to 1.7 μm , comprising 30 to 80% of the particle volume), and the carboxylic carbonyl group distribution was relatively more uniform than the other class of particles in which the carboxylic carbonyl was enriched at the surface. Such organic coatings significantly alter CCN behavior of the core material by reducing required supersaturations by as much as 0.2%, depending on the hygroscopicity of compounds in the outer layer relative to those comprising the core. In addition, texture analysis of particle images revealed uneven carboxylic carbonyl distributions across individual particles, sug-

gesting scenarios in which mechanistically derived mass accommodation coefficients may require careful interpretation. A little less than a quarter of the analyzed particles ($n = 142$) existed as an agglomeration or inclusion, or exhibited an uncategorized type of chemical heterogeneity.

[46] Notably, no occurrence of morphology or heterogeneity was confined to a single geographical location or field campaign. Such an observation underscores the similarities in source characteristics or atmospheric processing mechanisms leading to the observed variations in our particles. These morphologies and heterogeneities will affect aerosol optical properties, volatility, and water uptake in different ways and may be important to consider for satellite retrieval, measurement interpretation, or climate prediction.

[47] **Acknowledgments.** The authors acknowledge grant support for the analysis presented here from BP and for the particle samples collected for this work from DOE (W/GEC05-010 and MPC35TA-A5), NSF (ATM-0511772, ATM-0408501, ATM-0002035, ATM-0104707, ATM-0744636, and ATM-0904203), and the James S. McDonnell Foundation. In addition, valuable assistance was provided in using ALS facilities and interpreting NEXAFS spectra by A.L.D. Kilcoyne, T. Tyliszczak, M.K. Gilles, Ryan Moffet, and S. Gilardoni. R. Ramos, C. MacDonald, R. Leatch, L. Hawkins, D. Coffman, T.S. Bates, P.K. Quinn, and the science and operation teams of the field experiments of MILAGRO, INTEX-B, ICEALOT, Whistler, and VOCALS REx, and at the Scripps pier also provided enormous assistance in sample collection. The authors also thank G. Roberts for the code used for Köhler theory calculations and reviewers for helpful comments.

References

- Ackerman, T. P., and O. B. Toon (1981), Absorption of visible radiation in atmosphere containing mixtures of absorbing and non-absorbing particles, *Appl. Opt.*, **20**(20), 3661–3668.
- Adachi, K., and P. R. Buseck (2008), Internally mixed soot, sulfates, and organic matter in aerosol particles from Mexico city, *Atmos. Chem. Phys.*, **8**(21), 6469–6481.
- Ade, H., and S. G. Urquhart (2002), NEXAFS spectroscopy and microscopy of natural and synthetic polymers, in *Chemical Applications of Synchrotron Radiation*, edited by T. K. Sham, pp. 285–355, World Sci., Singapore.
- Aiken, A., et al. (2008), O/C and OM/OC ratios of primary, secondary, and ambient organic aerosols with high-resolution time-of-flight aerosol mass spectrometry, *Environ. Sci. Technol.*, **42**(12), 4478–4485.
- Alexander, D., J. Anderson, L. Forró, and P. Crozier (2008), The real carbon K-edge, *Microsc. Microanal.*, **14**(S2), 674–675.
- Bahadur, R., and L. M. Russell (2008), Water uptake coefficients and deliquescence of NaCl nanoparticles at atmospheric relative humidities from molecular dynamics simulations, *J. Chem. Phys.*, **129**(9), 094508.
- Baker, M., and R. Charlson (1990), Bistability of CCN concentrations and thermodynamics in the cloud-topped boundary layer, *Nature*, **345**, 142–145, doi:10.1038/345142a0.
- Bates, D. M., and D. Watts (1988), *Nonlinear Regression Analysis and Its Applications*, John Wiley, Hoboken, N. J.
- Bauer, S. E., and D. Koch (2005), Impact of heterogeneous sulfate formation at mineral dust surfaces on aerosol loads and radiative forcing in the Goddard Institute for Space Studies general circulation model, *J. Geophys. Res.*, **110**, D17202, doi:10.1029/2005JD005870.
- Bauer, S. E., M. I. Mishchenko, A. A. Lacis, S. Zhang, J. Perlwitz, and S. M. Metzger (2007), Do sulfate and nitrate coatings on mineral dust have important effects on radiative properties and climate modeling?, *J. Geophys. Res.*, **112**, D06307, doi:10.1029/2005JD006977.
- Bilde, M., and B. Svenningsson (2004), CCN activation of slightly soluble organics: The importance of small amounts of inorganic salt and particle phase, *Tellus, Ser. B*, **56**(2), 128–134.
- Bond, T. C., and R. W. Bergstrom (2006), Light absorption by carbonaceous particles: An investigative review, *Aerosol Sci. Technol.*, **40**(1), 27–67.
- Bond, T. C., G. Habib, and R. W. Bergstrom (2006), Limitations in the enhancement of visible light absorption due to mixing state, *J. Geophys. Res.*, **111**, D20211, doi:10.1029/2006JD007315.
- Braun, A. (2005), Carbon speciation in airborne particulate matter with C (1s) NEXAFS spectroscopy, *J. Environ. Monit.*, **7**(11), 1059–1065.
- Braun, A., F. E. Huggins, N. Shah, Y. Chen, S. Wirick, S. B. Mun, C. Jacobsen, and G. P. Huffman (2005), Advantages of soft X-ray absorption over TEM-EELS for solid carbon studies—A comparative study on diesel soot with EELS and nexafs, *Carbon*, **43**(1), 117–124.

- Braun, A., F. E. Huggins, A. Kubatova, S. Wirick, M. M. Maricq, B. S. Mun, J. D. McDonald, K. E. Kelly, N. Shah, and G. P. Huffman (2008), Toward distinguishing woodsmoke and diesel exhaust in ambient particulate matter, *Environ. Sci. Technol.*, **42**(2), 374–380.
- Braun, A., A. Kubatova, S. Wirick, and S. B. Mun (2009), Radiation damage from EELS and NEXAFS in diesel soot and diesel soot extracts, *J. Electron Spectrosc. Relat. Phenom.*, **170**(1–3), 42–48.
- Cappa, C. D., E. R. Lovejoy, and A. R. Ravishankara (2008), Evidence for liquid-like and nonideal behavior of a mixture of organic aerosol components, *Proc. Natl. Acad. Sci. U. S. A.*, **105**(48), 18,687–18,691.
- Chakraborty, P., and M. R. Zachariah (2007), “Effective” negative surface tension: A property of coated nanoaerosols relevant to the atmosphere, *J. Phys. Chem. A*, **111**(25), 5459–5464.
- Chakraborty, P., and M. R. Zachariah (2008), Sticking coefficient and processing of water vapor on organic-coated nanoaerosols, *J. Phys. Chem. A*, **112**(5), 966–972.
- Chan, M. N., and C. K. Chan (2005), Mass transfer effects in hygroscopic measurements of aerosol particles, *Atmos. Chem. Phys.*, **5**, 2703–2712.
- Chuang, P., R. Charlson, and J. Seinfeld (1997), Kinetic limitations on droplet formation in clouds, *Nature*, **390**(6660), 594–596.
- Corrigan, C., and T. Novakov (1999), Cloud condensation nucleus activity of organic compounds: A laboratory study, *Atmos. Environ.*, **33**(17), 2661–2668.
- Coz, E., F. Gómez-Moreno, M. Pujadas, G. Casuccio, T. Lersch, and B. Artíñano (2009), Individual particle characteristics of North African dust under different long-range transport scenarios, *Atmos. Environ.*, **43**(11), 1850–1863.
- Crutzen, P., and M. Andreae (1990), Biomass burning in the tropics: Impact on atmospheric chemistry and biogeochemical cycles, *Science*, **250**(4988), 1669–1678.
- Cruz, C., and S. Pandis (1998), The effect of organic coatings on the cloud condensation nuclei activation of inorganic atmospheric aerosol, *J. Geophys. Res.*, **103**(D11), 13,111–13,123.
- Decesari, S., M. Facchini, E. Matta, M. Mircea, S. Fuzzi, A. Chughtai, and D. Smith (2002), Water soluble organic compounds formed by oxidation of soot, *Atmos. Environ.*, **36**(11), 1827–1832.
- DeMott, P. J., K. Sassen, M. R. Poellot, D. Baumgardner, D. C. Rogers, S. D. Brooks, A. J. Prenni, and S. M. Kreidenweis (2003), African dust aerosols as atmospheric ice nuclei, *Geophys. Res. Lett.*, **30**(14), 1732, doi:10.1029/2003GL017410.
- Donaldson, D., A. Tuck, and V. Vaida (2001), Spontaneous fission of atmospheric aerosol particles, *Phys. Chem. Chem. Phys.*, **3**(23), 5270–5273.
- Dusek, U., G. Reischl, and R. Hitznerberger (2006), CCN activation of pure and coated carbon black particles, *Environ. Sci. Technol.*, **40**(4), 1223–1230.
- Feingold, G., and P. Chuang (2002), Analysis of the influence of film-forming compounds on droplet growth: Implications for cloud microphysical processes and climate, *J. Atmos. Sci.*, **59**(12), 2006–2018.
- Fuller, K. A., W. C. Malm, and S. M. Kreidenweis (1999), Effects of mixing on extinction by carbonaceous particles, *J. Geophys. Res.*, **104**(D13), 15,941–15,954.
- Gao, S., et al. (2004), Particle phase acidity and oligomer formation in secondary organic aerosol, *Environ. Sci. Technol.*, **38**(24), 6582–6589.
- Garland, E., E. Rosen, L. Clarke, and T. Baer (2008), Structure of submonolayer oleic acid coverages on inorganic aerosol particles: Evidence of island formation, *Phys. Chem. Chem. Phys.*, **10**(21), 3156–3161.
- Gilardoni, S., et al. (2007), Regional variation of organic functional groups in aerosol particles on four US east coast platforms during the International Consortium for Atmospheric Research on Transport and Transformation 2004 campaign, *J. Geophys. Res.*, **112**, D10S27, doi:10.1029/2006JD007737.
- Gilardoni, S., L. Shang, S. Takahama, L. M. Russell, J. D. Allan, R. Steinbrecher, J. L. Jimenez, P. F. Decarlo, E. J. Dunlea, and D. Baumgardner (2009), Characterization of organic ambient aerosol during MIRAGE 2006 on three platforms, *Atmos. Chem. Phys. Discuss.*, **9**, 6617–6655.
- Gonzalez, R., R. Woods, and S. Eddins (2003), *Digital Image Processing Using MATLAB*, Prentice-Hall, Upper Saddle River, N. J.
- Hamilton, J. F., P. J. Webb, A. C. Lewis, J. R. Hopkins, S. Smith, and P. Davy (2004), Partially oxidised organic components in urban aerosol using GCXGC-TOF/MS, *Atmos. Chem. Phys.*, **4**, 1279–1290.
- Haralick, R. M., K. Shanmugan, and I. Dinstein (1973), Textural features for image classification, *IEEE Trans. Syst. Man Cybern.*, **3**(6), 610–621.
- Hastie, T., R. Tibshirani, J. Friedman, and J. Franklin (2005), The elements of statistical learning: Data mining, inference and prediction, *Math. Intell.*, **27**(2), 83–85.
- Hill, S., A. Hill, and P. Barber (1984), Light scattering by size/shape distributions of soil particles and spheruloids, *Appl. Opt.*, **23**(7), 1025–1031.
- Hings, S. S., W. C. Wrobel, E. S. Cross, D. R. Worsnop, P. Davidovits, and T. B. Onasch (2008), CCN activation experiments with adipic acid: Effect of particle phase and adipic acid coatings on soluble and insoluble particles, *Atmos. Chem. Phys.*, **8**(14), 3735–3748.
- Hopkins, R. J., A. V. Tivanski, B. D. Marten, and M. K. Gilles (2007), Chemical bonding and structure of black carbon reference materials and individual carbonaceous atmospheric aerosols, *J. Aerosol Sci.*, **38**(6), 573–591.
- Hoppel, W., G. Frick, and J. Fitzgerald (1996), Deducing droplet concentration and supersaturation in marine boundary layer clouds from surface aerosol measurements, *J. Geophys. Res.*, **101**(D21), 26,553–26,565.
- Jacobson, M. Z. (2000), A physically-based treatment of elemental carbon optics: Implications for global direct forcing of aerosols, *Geophys. Res. Lett.*, **27**(2), 217–220.
- Jacobson, M. Z. (2001), Strong radiative heating due to the mixing state of black carbon in atmospheric aerosols, *Nature*, **409**(6821), 695–697.
- Jang, M., N. Zschocke, S. Lee, and R. Kamens (2002), Heterogeneous atmospheric aerosol production by acid-catalyzed particle-phase reactions, *Science*, **298**(5594), 814–817.
- Jasper, J. J. (1972), The surface tension of pure liquid compounds, *J. Phys. Chem. Ref. Data*, **1**, 841–1009.
- Johnson, K. S., B. Zuberi, L. T. Molina, M. J. Molina, M. J. Iedema, J. P. Cowin, D. J. Gaspar, C. Wang, and A. Laskin (2005), Processing of soot in an urban environment: Case study from the Mexico City Metropolitan area, *Atmos. Chem. Phys.*, **5**, 3033–3043.
- Kalberer, M., et al. (2004), Identification of polymers as major components of atmospheric organic aerosols, *Science*, **303**(5664), 1659–1662.
- Kandler, K., N. Benker, U. Bundke, E. Cuevas, M. Ebert, P. Knippertz, S. Rodriguez, L. Schütz, and S. Weinbruch (2007), Chemical composition and complex refractive index of Saharan mineral dust at Izaña, Tenerife (Spain) derived by electron microscopy, *Atmos. Environ.*, **41**(37), 8058–8074.
- Kandler, K., et al. (2009), Size distribution, mass concentration, chemical and mineralogical composition and derived optical parameters of the boundary layer aerosol at Tinfou, Morocco, during SAMUM 2006, *Tellus, Ser. B*, **61**(1), 32–50.
- Katrinarak, K. A., P. Rez, and P. R. Buseck (1992), Structural variations in individual carbonaceous particles from an urban aerosol, *Environ. Sci. Technol.*, **26**(10), 1967–1976.
- Kelly, J. T., C. C. Chuang, and A. S. Wexler (2007), Influence of dust composition on cloud droplet formation, *Atmos. Environ.*, **41**(14), 2904–2916.
- Kilcoyne, A., et al. (2003), Interferometer-controlled scanning transmission X-ray microscopes at the Advanced Light Source, *J. Synchrotron Radiat.*, **10**(2), 125–136.
- Kittelson, D., J. Johnson, W. Watts, Q. Wei, M. Drayton, D. Paulsen, and N. Bukowiecki (2000), Diesel aerosol sampling in the atmosphere, *SAE Tech. Pap. Ser.*, 2000-01-2212, 8 pp.
- Kocifaj, M., M. Gangl, F. Kundracik, H. Horvath, and G. Videen (2006), Simulation of the optical properties of single composite aerosols, *J. Aerosol Sci.*, **37**(12), 1683–1695.
- Kroll, J., and J. Seinfeld (2008), Chemistry of secondary organic aerosol: Formation and evolution of low-volatility organics in the atmosphere, *Atmos. Environ.*, **42**(16), 3593–3624.
- Kuwata, M., Y. Kondo, M. Mochida, N. Takegawa, and K. Kawamura (2007), Dependence of CCN activity of less volatile particles on the amount of coating observed in Tokyo, *J. Geophys. Res.*, **112**, D11207, doi:10.1029/2006JD007758.
- Laskin, A., J. Cowin, and M. Iedema (2006), Analysis of individual environmental particles using modern methods of electron microscopy and X-ray microanalysis, *J. Electron Spectrosc. Relat. Phenom.*, **150**(2–3), 260–274.
- Leaith, W. R., et al. (2009), Evidence for Asian dust effects from aerosol plume measurements during INTEX-B 2006 near Whistler, BC, *Atmos. Chem. Phys. Discuss.*, **8**, 18,531–18,589.
- Lerotic, M., C. Jacobsen, T. Schafer, and S. Vogt (2004), Cluster analysis of soft X-ray spectromicroscopy data, *Ultramicroscopy*, **100**(1–2), 35–57.
- Lerotic, M., C. Jacobsen, J. B. Gillow, A. J. Francis, S. Wirick, S. Vogt, and J. Maser (2005), Cluster analysis in soft X-ray spectromicroscopy: Finding the patterns in complex specimens, *J. Electron Spectrosc. Relat. Phenom.*, **144**, 1137–1143.
- Marcolli, C., and U. K. Krieger (2006), Phase changes during hygroscopic cycles of mixed organic/inorganic model systems of tropospheric aerosols, *J. Phys. Chem. A*, **110**(5), 1881–1893.
- Marcolli, C., B. P. Luo, and T. Peter (2004), Mixing of the organic aerosol fractions: Liquids as the thermodynamically stable phases, *J. Phys. Chem. A*, **108**(12), 2216–2224.
- Medina, J., and A. Nenes (2004), Effects of film-forming compounds on the growth of giant cloud condensation nuclei: Implications for cloud microphysics and the aerosol indirect effect, *J. Geophys. Res.*, **109**, D20207, doi:10.1029/2004JD004666.

- Mikhailov, E., S. Vlasenko, R. Niessner, and U. Poschl (2004), Interaction of aerosol particles composed of protein and salts with water vapor: Hygroscopic growth and microstructural rearrangement, *Atmos. Chem. Phys.*, **4**, 323–350.
- Minofar, B., M. Mucha, P. Jungwirth, X. Yang, Y. J. Fu, X. B. Wang, and L. S. Wang (2004), Bulk versus interfacial aqueous solvation of dicarboxylate dianions, *J. Am. Chem. Soc.*, **126**(37), 11,691–11,698.
- Mishchenko, M., A. Lacis, B. Carlson, and L. Travis (1995), Nonsphericity of dust-like tropospheric aerosols: Implications for aerosol remote sensing and climate modeling, *Geophys. Res. Lett.*, **22**(9), 1077–1080.
- Mishchenko, M., L. Travis, R. Kahn, and R. West (1997), Modeling phase functions for dustlike tropospheric aerosols using a shape mixture of randomly oriented polydisperse spheroids, *J. Geophys. Res.*, **102**(D14), 16,831–16,847.
- Mishchenko, M., L. Travis, and A. Lacis (2002), *Scattering, Absorption, and Emission of Light by Small Particles*, Cambridge Univ. Press, New York.
- Mishchenko, M. I., G. Videen, V. A. Babenko, N. G. Khlebtsov, and T. Wriedt (2004), T-matrix theory of electromagnetic scattering by particles and its applications: A comprehensive reference database, *J. Quant. Spectrosc. Radiat. Transfer*, **88**(1–3), 357–406.
- Mishchenko, M. I., G. Videen, V. A. Babenko, N. G. Khlebtsov, and T. Wriedt (2007), Comprehensive T-matrix reference database: A 2004–06 update, *J. Quant. Spectrosc. Radiat. Transfer*, **106**(1–3), 304–324.
- Moffet, R. C., X. Y. Qin, T. Rebotier, H. Furutani, and K. A. Prather (2008), Chemically segregated optical and microphysical properties of ambient aerosols measured in a single-particle mass spectrometer, *J. Geophys. Res.*, **113**, D12213, doi:10.1029/2007JD009393.
- Moussa, S. G., T. M. McIntire, M. Szori, M. Roeselova, D. J. Tobias, R. L. Grimm, J. C. Hemminger, and B. J. Finlayson-Pitts (2009), Experimental and theoretical characterization of adsorbed water on self-assembled monolayers: Understanding the interaction of water with atmospherically relevant surfaces, *J. Phys. Chem. A*, **113**(10), 2060–2069.
- O'Dowd, C., M. Smith, I. Consterdine, and J. Lowe (1997), Marine aerosol, sea-salt, and the marine sulphur cycle: A short review, *Atmos. Environ.*, **31**(1), 73–80.
- Okada, K., A. Kobayashi, Y. Iwasaka, H. Naruse, T. Tanaka, and O. Nemoto (1987), Features of individual Asian dust-storm particles collected at Nagoya, Japan, *J. Meteorol. Soc. Jpn.*, **65**(3), 515–521.
- Otsu, N. (1975), A threshold selection method from gray-level histograms, *Automatica*, **11**, 285–296.
- Paatero, P., and U. Tapper (1994), Positive matrix factorization—A non-negative factor model with optimal utilization of error-estimates of data values, *Environmetrics*, **5**(2), 111–126.
- Paatero, P., P. Hopke, X. Song, and Z. Ramadan (2002), Understanding and controlling rotations in factor analytic models, *Chemom. Intell. Lab. Syst.*, **60**(1–2), 253–264.
- Prisle, N., T. Raatikainen, R. Sorjamaa, B. Svenningsson, A. Laaksonen, and M. Bilde (2008), Surfactant partitioning in cloud droplet activation: A study of C8, C10, C12 and C14 normal fatty acid sodium salts, *Tellus, Ser. B*, **60**(3), 416–431.
- Reid, E. A., J. S. Reid, M. M. Meier, M. R. Dunlap, S. S. Cliff, A. Broumas, K. Perry, and H. Maring (2003), Characterization of African dust transported to Puerto Rico by individual particle and size segregated bulk analysis, *J. Geophys. Res.*, **108**(D19), 8591, doi:10.1029/2002JD002935.
- Roberts, G. C., P. Artaxo, J. C. Zhou, E. Swietlicki, and M. O. Andreae (2002), Sensitivity of CCN spectra on chemical and physical properties of aerosol: A case study from the Amazon basin, *J. Geophys. Res.*, **107**(D20), 8070, doi:10.1029/2001JD000583.
- Russell, L. M. (2003), Aerosol organic-mass-to-organic-carbon ratio measurements, *Environ. Sci. Technol.*, **37**(13), 2982–2987.
- Russell, L. M., S. F. Maria, and S. C. B. Myneni (2002), Mapping organic coatings on atmospheric particles, *Geophys. Res. Lett.*, **29**(16), 1779, doi:10.1029/2002GL014874.
- Russell, L. M., S. Takahama, S. Liu, L. Hawkins, D. S. Covert, P. Quinn, and T. S. Bates (2009), Oxygenated fraction and mass of organic aerosol from direct emission and atmospheric processing measured on the R/V *Ronald Brown* during TEXAQS/GoMACCS 2006, *J. Geophys. Res.*, **114**, D00F05, doi:10.1029/2008JD011275.
- Saathoff, H., K. H. Naumann, M. Schnaiter, W. Schock, O. Mohler, U. Schurath, E. Weingartner, M. Gysel, and U. Baltensperger (2003), Coating of soot and (NH₄)₂SO₄ particles by ozonolysis products of alpha-pinene, *J. Aerosol Sci.*, **34**(10), 1297–1321.
- Schumacher, M., I. Christl, A. C. Scheinost, C. Jacobsen, and R. Kretschmar (2005), Chemical heterogeneity of organic soil colloids investigated by scanning transmission X-ray microscopy and C-1s NEXAFS microspectroscopy, *Environ. Sci. Technol.*, **39**(23), 9094–9100.
- Seinfeld, J. H., and S. N. Pandis (2006), *Atmospheric Chemistry and Physics*, 2nd ed., John Wiley, Hoboken, N. J.
- Shi, Z. B., D. Z. Zhang, H. Z. Ji, S. Hasegawa, and M. Hayashi (2008), Modification of soot by volatile species in an urban atmosphere, *Sci. Total Environ.*, **389**(1), 195–201.
- Shilling, J. E., S. M. King, M. Mochida, and S. T. Martin (2007), Mass spectral evidence that small changes in composition caused by oxidative aging processes alter aerosol CCN properties, *J. Phys. Chem. A*, **111**(17), 3358–3368.
- Sjogren, S., M. Gysel, E. Weingartner, U. Baltensperger, M. J. Cubison, H. Coe, A. A. Zardini, C. Marcolli, U. K. Krieger, and T. Peter (2007), Hygroscopic growth and water uptake kinetics of two-phase aerosol particles consisting of ammonium sulfate, adipic and humic acid mixtures, *J. Aerosol Sci.*, **38**(2), 157–171.
- Sorjamaa, R., B. Svenningsson, T. Raatikainen, S. Henning, M. Bilde, and A. Laaksonen (2004), The role of surfactants in Kohler theory reconsidered, *Atmos. Chem. Phys.*, **4**, 2107–2117.
- Stöhr, J. (1992), *NEXAFS Spectroscopy*, Springer, Berlin.
- Sullivan, R. C., and K. A. Prather (2007), Investigations of the diurnal cycle and mixing state of oxalic acid in individual particles in Asian aerosol outflow, *Environ. Sci. Technol.*, **41**(23), 8062–8069.
- Takahama, S., S. Gilardoni, L. M. Russell, and A. L. D. Kilcoyne (2007), Classification of multiple types of organic carbon composition in atmospheric particles by scanning transmission X-ray microscopy analysis, *Atmos. Environ.*, **41**(40), 9435–9451.
- Takahama, S., S. Gilardoni, and L. M. Russell (2008), Single-particle oxidation state and morphology of atmospheric iron aerosols, *J. Geophys. Res.*, **113**, D22202, doi:10.1029/2008JD009810.
- Tervahattu, H., K. Hartonen, V. M. Kerminen, K. Kupiainen, P. Aarnio, T. Koskentalo, A. F. Tuck, and V. Vaida (2002a), New evidence of an organic layer on marine aerosols, *J. Geophys. Res.*, **107**(D7), 4053, doi:10.1029/2000JD000282.
- Tervahattu, H., J. Juhanaja, and K. Kupiainen (2002b), Identification of an organic coating on marine aerosol particles by TOF-SIMS, *J. Geophys. Res.*, **107**(D16), 4319, doi:10.1029/2001JD001403.
- Tervahattu, H., J. Juhanaja, V. Vaida, A. F. Tuck, J. V. Niemi, K. Kupiainen, M. Kulmala, and H. Vehkamäki (2005), Fatty acids on continental sulfate aerosol particles, *J. Geophys. Res.*, **110**, D06207, doi:10.1029/2004JD005400.
- Tivanski, A. V., R. J. Hopkins, T. Tyliczszak, and M. K. Gilles (2007), Oxygenated interface on biomass burn tar balls determined by single particle scanning transmission X-ray microscopy, *J. Phys. Chem. A*, **111**(25), 5448–5458.
- Tolocka, M., M. Jang, J. Ginter, F. Cox, R. Kamens, and M. Johnston (2004), Formation of oligomers in secondary organic aerosol, *Environ. Sci. Technol.*, **38**(5), 1428–1434.
- Turpin, B., and H. Lim (2001), Species contributions to PM_{2.5} mass concentrations: Revisiting common assumptions for estimating organic mass, *Aerosol Sci. Technol.*, **35**(1), 602–610.
- Urquhart, S. G., A. P. Hitchcock, A. P. Smith, H. W. Ade, W. Lidy, E. G. Rightor, and G. E. Mitchell (1999), Nexafs spectromicroscopy of polymers: Overview and quantitative analysis of polyurethane polymers, *J. Electron Spectrosc. Relat. Phenom.*, **100**, 119–135.
- Varga, Z., G. Kiss, and H. Hansson (2007), Modeling the cloud condensation nucleus activity of organic acids on the basis of surface tension and osmolality measurements, *Atmos. Chem. Phys.*, **7**, 4601–4611.
- Vincent, L. (1993), Morphological gray scale reconstruction in image analysis: Applications and efficient algorithms, *IEEE Trans. Image Process.*, **2**(2), 176–201.
- Wang, J., X. Liu, S. A. Christopher, J. S. Reid, E. Reid, and H. Maring (2003), The effects of non-sphericity on geostationary satellite retrievals of dust aerosols, *Geophys. Res. Lett.*, **30**(24), 2293, doi:10.1029/2003GL018697.
- Ward, J., Jr. (1963), Hierarchical grouping to optimize an objective function, *J. Am. Stat. Assoc.*, **58**, 236–244.
- Yoon, T., K. Benzerara, S. Ahn, R. Luthy, T. Tyliczszak, and G. Brown Jr. (2006), Nanometer-scale chemical heterogeneities of black carbon materials and their impacts on PCB sorption properties: Soft X-ray spectromicroscopy study, *Environ. Sci. Technol.*, **40**(19), 5923–5929.
- Zuberi, B., K. S. Johnson, G. K. Aleks, L. T. Molina, and A. Laskin (2005), Hydrophilic properties of aged soot, *Geophys. Res. Lett.*, **32**, L01807, doi:10.1029/2004GL021496.

S. Liu, L. M. Russell, and S. Takahama, Scripps Institution of Oceanography, University of California, San Diego, Department 0221, La Jolla, CA 92093, USA. (liushang@ucsd.edu; lmrussell@ucsd.edu; stakahama@ucsd.edu)